Transport and Morphology of a Proton Exchange Membrane Based on a Doubly Functionalized Perflourosulfonic Imide Side Chain Perflourinated Polymer

Ahmet Kusoglu,[a] *Keti Vezzù,* [b,c,d] *Govind Hegde,*[e] *Graeme Nawn,*[b,d] *Andrew R. Motz,*[e] *Himanshu N. Sarode,*[e] *Gregory M. Haugen,*[f] *Yuan Yang,*[g] *Soenke Seifert,*[h] *Michael A. Yandrasits,*[f] *Steven J. Hamrock,*[f] *C. Mark Maupin,*[e] *Adam Z. Weber,*[a] *Vito Di Noto,**, [b,i] *and Andrew M. Herring.**,[e]

[a] Energy Conversion Group, Lawrence Berkeley National Laboratory, Berkeley CA 947203, USA

[b] Section of Chemistry for Technology, Department of Industrial Engineering, University of Padova, Via F. Marzolo 9, I-35131 Padova, Italy

[c] INSTM, Via Gradenigo 6/A, I-35131 Padova, Italy

[d] Centre for Mechanics of Biological Materials (CMBM), Via F. Marzolo 9, I-35131 Padova, Italy

[e] Department of Chemical and Biological Engineering, Colorado School of Mines, Golden, CO 80401, USA

[f] 3M Energy Components Program 3M Center, St. Paul, MN 55144, USA

[g] Department of Chemistry and Geochemistry, Colorado School of Mines, Golden, CO 80401, USA

[h] X-Ray Sciences Division, Advanced Photon Source, Argonne National Laboratory, Argonne, IL, USA

[i] Department of Materials Science and Engineering and Chemical Engineering, University Carlos III of Madrid, 28911 Leganes, Madrid, Spain.

Abstract. There is a critical need for higher performing proton exchange membranes for electrochemical energy conversion devices that would enable higher temperature and drier operating conditions to be utilized. A novel approach is to utilize multi-acid side chains in a perfluorinated polymer, maintaining the mechanical properties of the material, whilst dramatically increasing the ion-exchange capacity; however, as we show in this paper, the more complex side chain gives rise to unexpected physical phenomena in the material. We have thoroughly investigated a doubly functionalized perfluorosulfonic imide-acid side chain perfluorinated polymer (PFIA), the simplest of many possible multi-acid side chains currently being developed. The material is compared to its simpler perfluorosulfonic-acid (PFSA) analogue via a battery of characterization and modeling investigations. The doubly functional side chain profoundly influences the properties of the PFIA polymer as it gives rise to both inter- and intra- side chain interactions. These affect the nature of thermal decomposition of the material, but more importantly force the backbone of the polymer into an unusually highly ordered more crystalline configuration. Under water saturated conditions, the PFIA has the same proton conductivity as the PFSA material, indicating that the additional proton does not contribute to the ionic conductivity, but the PFIA shows higher proton conductivity at lower RH conditions owing to dynamic changes in its local molecular environment. A transition is observed between 30 and 60 °C, indicating an order/disorder transition that is not present in the PFSA analogue. The mechanism of proton transport in the PFIA is due to more delocalized protons and more flexible side chains with better-dispersed, smaller water clusters forming the hydrophilic domains than in PFSA analogue.

INTRODUCTION

With the world's population at >7 billion people and the $CO_{2(g)}$ concentration in the atmosphere at > 400 ppm threatening globally destructive climate change, there is an immediate need to move to more efficient carbon-free energy-conversion systems.[1] With Toyota's introduction of the Mirai H_2 fuel-cell powered automobile, this is rapidly becoming a reality, assuming that low-cost routes to renewable H_2 can be achieved.[2] Whereas the Mirai represents a first-generation commercial product, there are still many challenges to driving down the cost and increasing the durability and performance of such vehicles. One of these challenges is improving the performance of the proton exchange membrane (PEM), which is the solid-electrolyte separator in the fuel cell. Currently, the incumbent PEM is a perfluorosulfonic acid copolymer (PFSA) supported with an expanded-polytetraflouroethylene (e-PTFE) network.[3] The most common PFSA is Nafion® (Figure 1), which has poor proton conducting performance when not saturated by water, thereby requiring operation below 100°C, as higher temperatures require unpractical levels of pressurization to maintain higher hydration and hence useful proton conductivity.[3a] The consequence of this is the need for complicated water and thermal humidification and heat-rejection systems. Therefore, there is still a need for materials with even higher proton conductivities than the incumbent polymers, especially under hotter and drier operating conditions. Thus, understanding and improving the ion-transport in PFSA ionomers and their analogues have been of great interest in the scientific community with direct implications for various energy-conversion technologies.

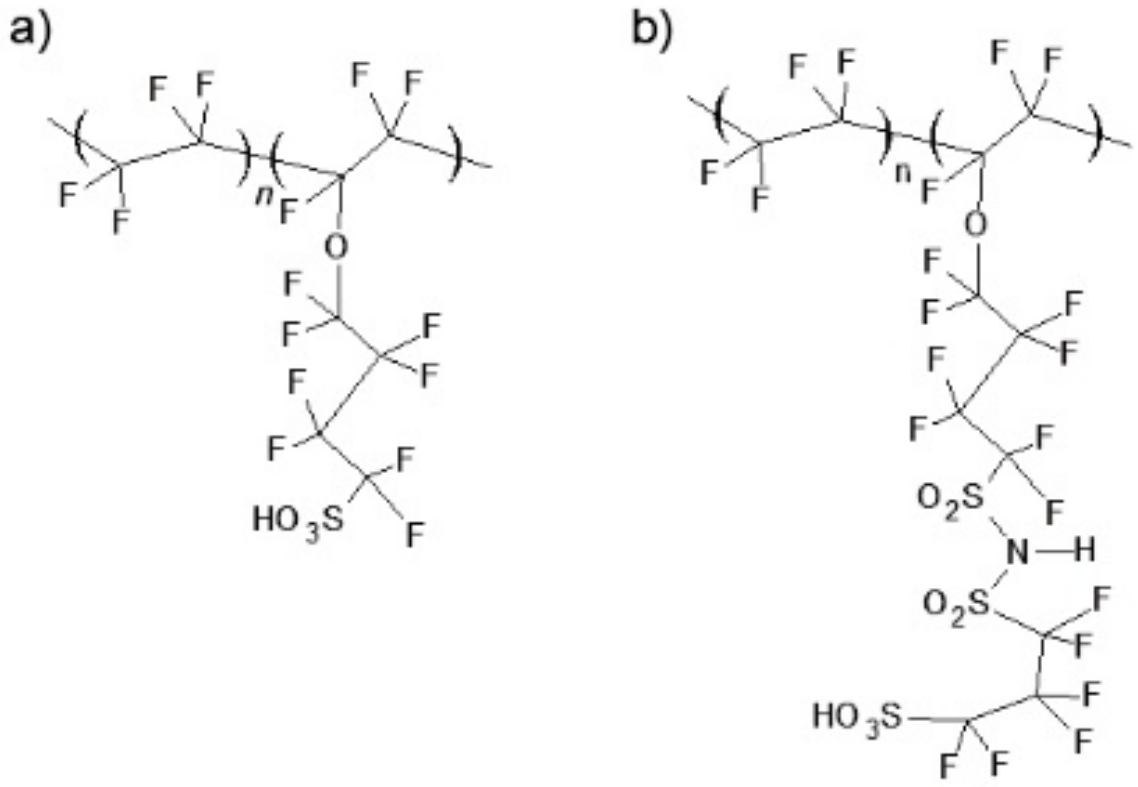

Figure 1. Chemical structure of PFSA (a) and PFIA (b). n = 4 – 5.

The cell performance is directly related to the membrane's transport properties, which are governed by the ionomer's chemistry including equivalent weight (EW) (or ion-exchange capacity, IEC) and side chain chemistry, physicochemical state and morphology, as well as environmental conditions. In particular, proton transport in the PFSAs is governed by a multitude of complex mechanisms occurring across length scales, including dissociation of protons from acidic end groups and their transport through water domains facilitated by polymer matrix relaxations.

PFSA morphology is driven by hydration, which results in growth and connectivity of the hydrophilic domains that enable facile proton and water transport.[3a] However, the disordered nature of PFSA ionomers combined with the presence of distinct mechanisms governing transport at molecular scale

(proton dissociation and relaxations of the polymer matrix), nano-scale (transport within water domains) and mesoscales (network tortuosity, polymer dynamics and long-range transport) results in a multi-scale transport phenomenon. While the water-ion interactions within the proximity of polymer sulfonate ions and the relaxations of the polymer matrix are more dominant at smaller lengthscales, morphology-driven transport and mesoscale polymer dynamics become more influential at larger lengthscales. Increasing hydration impacts these mechanisms at all lengthscales by: (i) enhancing proton dissociation; (ii) accelerating relaxation times of polymer matrix dynamics (plasticization of the matrix); and (iii) reducing network tortuosity, thereby improving domain interconnectivity to promote more facile water-ion transport.[3a, 4] It was inferred that conductivity is not solely impacted by the hydration, but also influenced by the polymer-chain structure and conformation, as shown in studies on transport,[4d, 5] dielectric spectroscopy,[5a, 6] NMR[4d, 7] and molecular modeling,[8] pointing out the roles of backbone and side chain conformation in transport and the favorable impact of shorter backbone on better-dispersed domains. The role of lower EW in enhancing proton mobility at the same λ was attributed to the formation of more continuous water network, wherein the associated bound water molecules are loosened due to the closely-spaced sulfonate groups,[4d] thereby increasing the mobility by enhancing formation of water-sulfonate bridges and stabilizing the hydrogen-bond network.[8a, 8i-k, 9] It must be pointed out that lower-EW PFSAs possess shorter side chains compared to Nafion®, influencing proton dissociation[8b-d, 8g, 10] and transport,[5, 7c, 11] the effect of which becomes apparent at lower RHs, where the proton transport relies on the hydronium bridges between sulfonate sites and side chain.[8g, 8i, 12]

While lowering EW, and therefore increasing the molar acid content, enhances the membrane's proton conductivity, it also negatively impacts its stability by shortening the fluoropolymer backbone chain, resulting in a transport/stability tradeoff. One strategy to overcome such detrimental effects in low-EW PFSAs is to alter the side chain chemistry, while maintaining the same stable backbone. It has been

documented in the literature that PFSAs with a shorter side chains could exhibit higher conductivity at a given relative humidity (RH), which is related to their ability to attain higher water content and IECs with efficient chain packing without sacrificing stability compared to their Nafion analogue. In a recent study, Giffin *et al.*[5a] showed that EW affects the hopping- and proton-conduction mechanisms, which are accompanied by changes in the crystallinity and conformation of the PTFE backbone, indicating the critical role of EW in facilitating proton transport and controlling the structure/function relationship. Molecular-Dynamics (MD) simulations suggest that short(er) side chain ionomers have improved backbone flexibility, which enhances the proton dissociation and leads to higher conductivity.[8c-e] This improvement stems from the work of Agmon,[13] where structural diffusion of proton hopping was described via a series of bond breaking and forming steps transfer protons across the hydrogen-bond network,[4a, 14] which occurs on the order of ps.[13] Such a hopping mechanisms is thus tightly correlated to solvation phenomena and ion distances to enable reorientation of water molecules, and therefore is thought to be more dominant at higher hydration conditions.[4a, b, 15] While these aspects were initially explored in aqueous environments by Tuckerman *et al.*,[16] more recent explorations point to the fact that water exists in a bulk-like structure in the center of a domain where transport is facilitated by proton hopping, whereas, at the polymer/water interface (within < 1 nm of pore wall), transport is vehicular in nature.[17] The simulations revealed that when the backbone is folded partially, it brings sequential SO_3^- groups closer, thereby allowing water to bind strongly to the protogenic groups. Such transport may well be altered by different molecular and water-domain configurations, where for example, proton dissociation was found to increase as the distance between the SO_3H groups decreased.[18]

FT-IR ATR and micro-Raman vibrational investigations allowed to obtain information on the structure of the hydrophobic polytetrafluoroethylene domains of PFSA and on the interactions polymer– polymer, polymer –[nanofiller] and polymer–[H_2O] in bulk materials. In particular, vibrational studies of the CF

region revealed that the fluorocarbon chains of hydrophobic PTFE domains of PFSA membranes consist of a blend of 2_1, 15_7, 10_3, and 4_1 helices.[5a, 19] It was highlighted that the mesoscale structural reorganization of these conformational chains play a crucial role in modulating the microscopic morphology of bulk membranes. Indeed, the EW is a crucial parameter in the modulation of the helical conformation of backbone chains and therefore of the composition of the chain blends in PTFE domains of PFSA membranes. In addition, this investigation demonstrated that the hydrophobic domains of PFSA membranes mainly consists of a blend of 15_7, 10_3 conformational chains which: a) in Nafion is predominated by the concentration of 15_7; and b) in 3M membrane at 825 EW by the 10_3, while for all of the other higher EW membranes by the 15_7 helix.[5a, 19]

The combination of MD and FT-IR spectral analysis allowed to get a closer look at water in the hydrophilic domains of PFSA membranes. Particularly, ATR FT-IR studies in the range 1560-2000 cm^{-1} revealed four different species of water clusters embedded inside polar domains and their interconnecting channels: (a) bulk water $[(H_2O)_n]$; (b) water solvating the oxonium ions directly interacting with sulfonic acid groups $[H_3O^+\cdots SO_3^-]\cdot(H_2O)_n$; (c) water aggregates associated with H_3O^+ ions $[H_3O^+\cdot(H_2O)_n]$; and (d) low associated water species in dimer form $[(H_2O)_2]$.[6a, 20] The latter two water species are present in both the Nafion hydrophilic domains and their interconnecting channels. These studies permitted to distinguish the physicochemical behavior of the structural reorganizations of water molecules in the *"surface"* of the polymer domains as opposed to *"bulk"* water molecules embedded in the hydrophilic cavities of the membranes.[21]

Investigation of the electrical response of PFSA membranes by Broadband Electrical Spectroscopic (BES) revealed that the long-range charge migration mechanism (*i.e.*, the overall conductivity, $\sigma_T = \sigma_{EP}$

+ σ_{IP}) is the superposition of two distinct conductivity mechanisms: the material's interdomain (σ_{IP}) and the bulk proton conduction pathway (σ_{EP}).[22] It was demonstrated that σ_{EP} is a long-range conduction pathway which occurs when the proton is exchanged between different delocalization bodies (DB). For definition a DB was identified with a wetted sub micro metric volume of a membrane, which includes all its components (the hydrophobic and the hydrophilic domains and if there is any the nanofiller particles) where the proton, with respect to the time scale of the overall conductivity, is exchanged between coordination sites so fast to be considered delocalized. Therefore, the long-range migration process occurs when different DBs exchange the proton at the characteristic time of the overall conductivity by coming into contact following the fluctuations/segmental motion of the hydrophobic domains of the PFSA host matrix.[22] It was reported that σ_{IP} consists of an interdomain proton conduction pathway which occurs when the proton is exchanged between ligand coordination sites distributed along the interface between the hydrophobic and hydrophilic domains. It was revealed that in general in wetted PFSA membranes σ_{EP} is 2-4 orders of magnitude higher than σ_{IP}, thus $\sigma_T = \sigma_{EP} + \sigma_{IP} \approx \sigma_{EP}$.[23]

Changes in transport mechanisms with EW also imply a change in the water-domain network. Nevertheless, when the conductivity is compared at the same water content, the improvements become relatively minimal, especially at lower RH (see a recent review for details).[3a] Thus, there is a need to explore alternative side chain chemistries that could promote better proton transport at the same water content. One strategy that has shown promise in improving PFSA performance in harsh environments and possibly breaks the PFSA conduction mechanism and paradigm is increasing the number of protogenic groups on the side chain (for the same backbone), so-called multi-acid side chain (MASC) ionomers, developed by 3M.[24] These polymers are based on a medium chain sulfonyl fluoride.[25] One particular chemistry is perfluoro imide acid (PFIA), which shares the same fluorocarbon backbone as the PFSA, but contains an additional imide acid group providing the secondary protogenic group (Figure 1).

The 3M PFSA is synthesized by hydrolyzing the sulfonyl fluoride to the sulfonic acid (Figure 1a). However, the sulfonyl fluoride may also be converted to the PerFluoro Imide Acid (PFIA) (Figure 1b) that has two dissociable protogenic groups.[24] This approach has the advantage that for the same number of PTFE groups (n) needed for structural integrity along the backbone, two acid groups can be introduced allowing a lower EW polymer with similar strength and water stability as the equivalent PFSA. In this case, starting with the same sulfonyl fluoride polymer, the PFSA generated would have an EW of 825 g/mol, but the PFIA would have an EW of 583 g/mol at 100% conversion. This important material is being developed by 3M because of its dramatically higher proton conductivity at lower RHs than the parent PFSA, which results in improved performance in fuel cells when run under hotter and drier conditions.

As noted above, proton dissociation and the number of water molecules required to enact proton dissociation is directly impacted by the backbone length of the side chains: the shorter this backbone, the lower the number of water molecules required to transfer protons to the hydration shell of water.[8c, d, 26] Thus, the backbone conformation of side chains and the proximity of the acidic groups are strongly intertwined and influence proton transport.[8c, d] It was shown that heating a membrane up to 160 °C results in a broader distribution of less conductive sites, reminiscent of dehydration effects.[27] However, temperature-dependences of such effects could be different as the 3M PFIA was shown to retain slightly higher hydrophilicity at elevated temperatures, in line with its more conductive nature, despite its similar atomic-force-microscopy (AFM) profiles at lower temperatures compared to PFSAs.[27] From AFM studies, larger hydrophilic domains of 7-8 nm in size have been inferred for PFIA.[27]

The work in this paper is aimed at developing an understanding of the details of proton transport and why it is improved for the PFIA and the implications on polymer properties of the bi-functional side

chain. Throughout the paper, we compare the PFIA to the PFSA built from the same perfluorsulfonyl fluoride so that the only variation is the side chain of the polymer and the PTFE backbone length remains constant. We start by assessing the through-plane and in-plane proton conductivity of the material as a function of temperature and RH. Water uptake is measured by dynamic vapor sorption (DVS) and is used to normalize the proton conductivity to water content. Next, we assess the mechanical properties of the polymer by thermogravimetric analysis (TGA), modulated differential scanning calorimetry (MDSC), dynamic mechanical analysis (DMA), and extensional rheometry under RH control. From these measurements, we have a complete picture of the material's ionic and mechanical performance. We use infrared (IR) spectroscopy to study the structural features of the materials and the unique chemical interactions of the side chains and an extensive small- and wide-angle X-ray scattering (SAXS and WAXS) study to shed light on to the nanostructure of the polymer morphology. Finally, broadband electric spectroscopy (BES) data and MD calculations are used to elucidate and confirm the origin of the mechanical properties and the mechanism of proton conduction in PFIA.

EXPERIMENTAL

MATERIALS. PFIA membranes from 3M Company were prepared as previously described.[24] Membranes were fabricated by casting from a dispersion in ethanol and water (75:25 vol%) that was cast onto an inert liner, dried at 140°C, and then subsequently annealed at 200°C in air. The films were cleaned by boiling in 4 separate solutions for 1 hr each, in succession: hydrogen peroxide (3-wt% hydrogen peroxide in water), deionized (DI) water (18 MΩ), sulfuric acid (0.5 M), and DI water. Membranes were rinsed with DI water following each step and stored in DI water in the dark.

CONDUCTIVITY MEASUREMENTS – THROUGH-PLANE. The through-plane conductivity was measured as a function of RH and temperature via AC impedance measurements using a Membrane Test

System (MTS) (MTS740, Scribner Associates, Inc.) equipped with an SI 1260 impedance/gain-phase analyzer (Schlumberger Technologies, Inc.) and ZPlot software (Scribner Associates, Inc.). Membranes were cut into a rectangular piece with the dimension of 10 mm by 30 mm and were sandwiched between gas-diffusion layers (GDLs) (SGL 10BC). The GDLs were attached to the platinum source electrode with conductive carbon paint. The assembly was compressed with a load of approximately 2.15 MPa measured by a calibrated force spring and dial displacement indicator. Samples were first kept at 70% RH and 30°C under nitrogen atmosphere for 2 hours at the beginning of the test. Afterward, samples were dried to 20% RH with a step of 10% RH, and then hydrated to 90% with an increment interval of 10% RH, then to 95% and 98% RH. The through-plane conductivity was calculated as $\kappa = L/RA$, where L is the thickness of the membrane measured at ambient conditions, R is the resistance derived from the intercept of the high-frequency impedance with the real axis, and A is the overlapping area of the platinum source electrodes (0.5 cm^2).

WATER UPTAKE. Membrane water uptake as a function of RH was measured by DVS (Surface Measurement Systems, UK) at 25, 30, 60, and 85°C. First, the samples were dried in the DVS at 0% RH and 25°C for 2 hours to set an initial state for sample weight. The samples were then humidified from 0 to 90% RH with an increasing RH interval of 10%, and then to 98% RH. Samples were dehumidified back to 0% RH following the same RH values and interval, but in the opposite sequence. Water uptake of the membrane, ΔM_w, was continuously determined from the weight change with respect to the sample's dry weight, M_0, which was determined after heating the sample to 120°C. At each RH step, the samples were equilibrated for a minimum of 2 hours or until the change in the sample weight, $\Delta M_w/M_0$, was less than 0.005 %/min. The average of sorption and desorption values were taken at each humidity. The water content, λ, the number of water molecules per acid group of ionomer, is calculated based on the water uptake, $\Delta M_w/M_0$ as:

$$\lambda = \frac{mol(\mathrm{H_2O})}{mol(\text{acid group})} = \frac{\Delta M_w / 18}{M_0 / EW'} \qquad (1)$$

where EW is also defined as weight polymer per acidic group in g/mol and the molecular weight of the water is 18 g/mol. EW is determined as elsewhere reported.[28]

TGA. TGA analyses were carried out using a high-resolution thermobalance TGA 2950 (TA Instruments) under either a nitrogen or dry air flow, at a rate of 100 cm^3 min^{-1}. The sensitivity of the instrument is in the range of 0.1 to 2 % min^{-1} and the resolution is 1 μg. TGA profiles are collected over a temperature range between 25 and 950°C with the heating rate varied from 40 to 0.001°C min^{-1}, depending on the first derivative of the weight loss. Approximately 3 mg of sample was loaded onto an open platinum pan. The dry samples were prepared inside a glove box under an argon atmosphere and the entire analyzer was mounted inside a nitrogen filled glove bag.

MDSC. Modulated Differential Scanning Calorimetry (MDSC) analyses were performed using a DSC Q 20 (TA Instruments) equipped with a liquid nitrogen cooling system. Measurements were carried out using a modulated mode over a temperature range of -150 to 350°C, with a ± 1°C modulation every 60 seconds. Approximately 4 mg of sample was loaded inside a hermetically-sealed aluminum pan. Dry samples were prepared inside a glovebox under an argon atmosphere.

FTIR-ATR. Fourier Transform – Infra Red Attenuated Total Reflectance (FTIR-ATR) spectra were collected using a Nicolet FT-IR Nexus spectrometer with a resolution of 2 cm^{-1}. The spectra for PFIA samples were obtained in Single-Bounce ATR mode using a Golden Gate accessory (Specac) in the mid-infrared (MIR) range. The spectra for PFSA samples were obtained in the ATR mode using a Perkin-Elmer Frustrated Multiple Internal Reflections 186-0174 accessory. Dry samples were prepared inside a glovebox under an argon atmosphere.

BROADBAND ELECTRICAL SPECTROSCOPY (BES). BES data are collected over the frequency range of 0.1 Hz to 1 MHz using a Novocontrol Alpha Analyzer. The electric spectra were measured in the

thermal range between -105 and 195 °C using 10 °C intervals with accuracy greater than ± 0.1 °C. The temperature was controlled with a cryostat equipped with a gaseous nitrogen heating-cooling system. Circular samples of diameter 13 mm were compressed between two platinum cylindrical electrodes. Dry samples were prepared inside a glovebox under an argon atmosphere and wet membranes were measured in twice deionized water.

SMALL- AND WIDE-ANGLE X-RAY SCATTERING (SAXS/WAXS). X-ray scattering experiments were conducted at the Advanced Photon Source (APS) on beamline 12-ID-C and at the Advanced Light Source (ALS), beamline 7.3.3. The experiments at the APS were conducted in an environmental chamber with control over temperature and humidity, and was verified to be constant by a calibrated Visala HMT337 humidity transmitter; more detailed description of the custom-built chamber has been previously reported.[29] The conditions of the chamber will be described throughout the text and range from 0 to 95% RH and 30 to 90 °C. The energy of the beamline was 12 keV with a wavelength of 1 Å. For the humidity sweep, the membrane was first allowed to equilibrate at 60 °C and 0% RH, and then RH was increased sequentially up to 95% RH. After the membrane was equilibrated at 0% RH, a step change in RH was made to 25% RH and data was taken every 5 minutes until the membrane reached equilibrium, at least 1 h. This was repeated for 50, 75, and 95% RH. For the temperature sweep, the film was allowed 1 h to equilibrate at the initial condition, data was then collected, followed by a 10 °C increase in temperature. After the chamber reached each condition, the membrane was allowed to equilibrate until no further changes were observed. This process was repeated for the whole temperature range. SAXS/WAXS experiments at the ALS were carried out using computer-controlled heating stage containing liquid-solution cells allowing imaging *"in-situ"*. Experimental details are provided elsewhere.[30] The samples were tested either in DI water or dry, and scattering patterns were collected at different temperatures. The X-ray energy was 10 keV, and wavelength was 0.124 nm with a monochromator energy resolution, E/dE, of 100, and the patterns were acquired with a two-dimensional (2D) Dectris Pilatus 2M CCD

detector (172 μm x 172 μm pixel size). The scattering wave vector, $q = 4\pi \sin(\theta)/0.124$, ranged from 0.008 to 0.04 $Å^{-1}$ for SAXS and extended up to 4 $Å^{-1}$ for WAXS, where θ is the scattering angle. For all the collected patterns, intensity *vs.* scattering wave vector (I(*q*)) profiles were obtained from the radial integration of 2D images and corrected for background scattering.

MOLECULAR-DYNAMICS CALCULATIONS. MD simulations of periodic entangled polymer systems at varying hydration levels and temperatures were conducted using the program AMBER14.[31] To investigate the effect of hydration level and temperature on the behavior of the PFIA membranes and facilitate comparison with experiments, λ values of 1, 5, 15, and 20 were simulated at temperatures of 25, 60, 80, and 125 °C. The systems consisted of TIP3P[32] water, classical hydronium ions and the PFIA polymer chains. The classical hydronium cations (H_3O^+) were modeled based on the force field used in previous work,[33] while a charge modified generalized AMBER force field was used to describe the polymer.[33c, 34] To calculate the charges, the PFIA monomer was optimized at the B3LYP/6-311G(2d,d,p) level of theory and basis set using the Gaussian 09 program,[35] followed by a single point calculation at the HF/6-311G(2d,d,p) level of theory and basis set. The charges were then calculated using RESP[36] and antechamber[37] in accordance with previous publications.[33c, 38] Initial construction of the entangled polymer systems was performed using an in-house Monte Carlo chain-growing algorithm that allowed for precise specification of the length, number, and composition of polymer chains.[33c, 39] The entangled systems were then solvated with the program Packmol[40] to insert the classical hydronium molecules (one for each acid group in the system) and the appropriate number of water molecules to obtain the desired hydration level. Systems were subjected to an initial minimization of 10000 steps using the steepest descent algorithm followed by 10000 steps of conjugated gradient geometry optimization. The systems were then subjected to a cycling process, which consisted of alternating between 500 ps in the isobaric isothermal (NPT) ensemble at 1 atm pressure and 298 K, and 500 ps in the canonical (NVT) ensemble at 500 K. The cycling was performed until no significant change in density was observed in the NPT

simulations. All systems were then equilibrated for 500 ps in the NPT ensemble at the desired production temperature before running the NVT and NVE ensemble production runs. The production runs consisted of 5 ns in the NVT ensemble for structural property calculation and 20 ns in the NVE ensemble for diffusion and dynamic property calculation.

RESULTS AND DISCUSSION

CHARACTERIZATION OF THE BASE NANOSTRUCTURE. We first discuss the thermal behavior of the two polymers. To understand their intrinsic nanomorphology, various studies of the dry systems are carried out to highlight the differences in the two side chains and their respective effects on the polymer backbone. The thermal stability and transitions of the PFIA are compared to the PFSA in their dry states by TGA and MDSC in Figure 1. The small mass loss (I), occurring at temperatures below 200 °C and present in the profiles of both PFIA and PFSA, is attributed to the elimination of traces of water and possibly decomposition of side chain termini sulfonate-group moieties. A two-step mass elimination process then follows, beginning at 360 °C for PFIA and 390 °C for PFSA (II). The first part of this two-step process (II) is attributed to the thermal decomposition of the respective side groups.[6a, 28, 41]

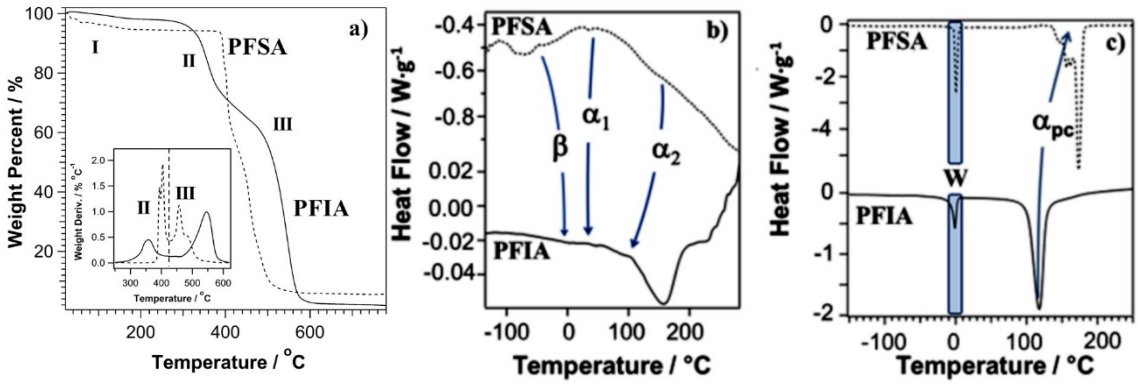

Figure 1. (a) HR-TGA profiles of PFIA (solid line) and PFSA (dashed line), with HR-TGA profiles as a function of weight derivative (inset). All analyses were carried out in a nitrogen atmosphere. MDSC

profiles of PFIA (solid line) and PFSA (dashed line) presented as total heat flow in (b) dry state and (c) wet state.

The second part of the two-step decomposition (III) is attributed to the thermal decomposition of the PTFE backbone itself, and occurs at 542 °C for the PFIA, and 455 °C for the PFSA.[5a, 6a, 28, 41] This suggests that, in the PFIA, the elimination of side functionalities occurs through elimination processes A and B shown in Scheme 1. These latter result in the dynamic crosslinking interactions occurring between the perfluorinated side groups, which stabilize the resulting hydrophobic polymer network. As Scheme 1 shows inter- or intra-side chain interactions occur in the PFIA owing to $(R–SO_2–)_2N–H \cdots HSO_3–R$ and $(R–SO_2–)_2NH_2^+ \cdots {}^-SO_3–R$ type interactions that stabilize the pristine polymer below 200 °C and reduce the temperature of the side chain degradation in process II, compared to PFSA. We hypothesize that in the pristine PFIA, a mixture of intra- and inter-side chain interactions are present where intra-side chain interactions occur as shown in Scheme 1a, while inter-side chain interactions take place according to Scheme 1b. On this basis, the PFIA has a lower degradation temperature than the PFSA due to processes 1 and 2 (Scheme 1). The thermal stability of the side chains is reduced as the degradation of the sulfonyl imide functionalities produces volatile species that are easily eliminated. This then promotes the thermal crosslinking that renders degradation event III for PFIA at higher temperature than that observed for the PFSA, thereby suggesting that flexibility of the PFIA side chains is higher than that of the PFSA ones, resulting in a distribution of conformations that help delocalize the protons.

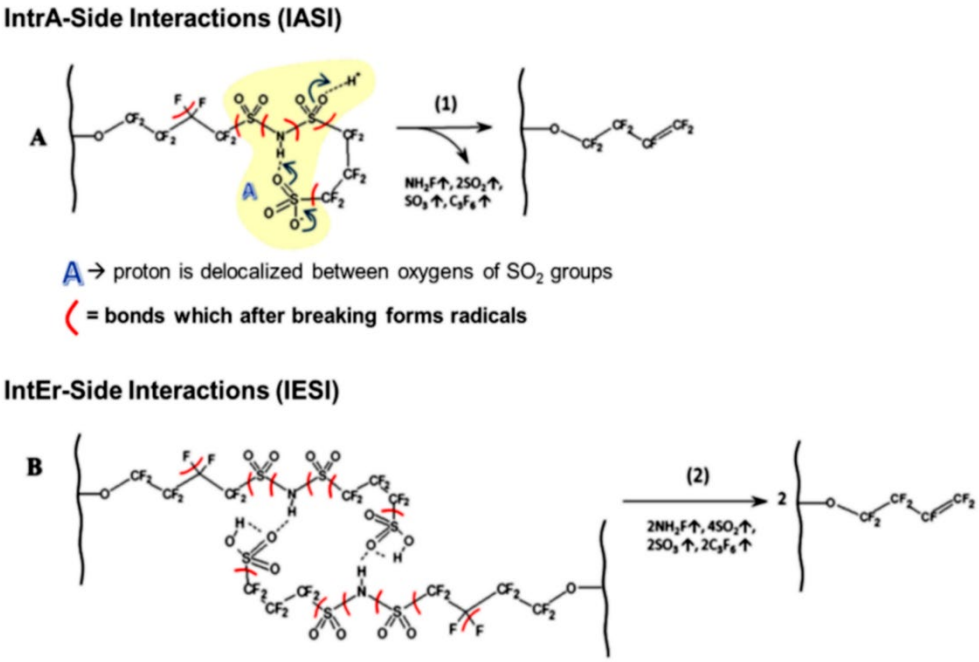

Scheme 1. Intra- and inter-side chain interactions between PFIA side chains, where A and B show models of the hypothetical intra- and inter-chain interactions, respectively. The models are supported by thermoanalytical and FT-IR ATR studies (see text). (1) and (2) show a scheme of the elimination process (II of the HR-TGA profiles, see Figure 2), confirmed by the FT-IR analysis of degradation gases (data not shown).

The above schemes are also consistent with the MDSC results in Figure 1b, where both the PFIA and PFSA exhibit a subzero temperature thermal event, β, that occurs at *ca.* –18 and *ca.* –45 °C for the PFIA and PFSA, respectively. This event is likely associated with the ether moiety at the junction between the side chains and the polymer backbone.[42] The slight increase in the temperature of the β transition for the PFIA with respect to the PFSA may be due to a more hindered motion around the ether connections. A second thermal event, α_1, that occurs largely in the same region for both materials, *i.e.*, 40 to 50 °C, is assigned to an order/disorder conformational transition attributed to the 13_6 to 15_7 CF_2 helical transitions of the PTFE backbone chains.[28, 41, 43] A final relaxation phenomena, α_2, is observed at *ca*. 100 °C for both

the PFIA and PFSA, and is associated with the segmental motions of the PTFE backbone chains[35-36] (*i.e.*, diffusion of conformational states along perfluorinated backbone chains in the hydrophobic domains). The melting transition of the PTFE hydrophobic domains (T_m) of the PFIA is observed at *ca.* 150 °C, whereas that of the PFSA occurs outside of the available temperature range of the instrument.[22] In addition, MDSC of the wet membranes demonstrated two thermal events for both membranes, labeled as W and α_{pc} in Figure 2c. For both PFIA and PFSA, the W transition occurs at 0 °C and is attributed to the melting of the water in the hydrophilic domains.[5a, 6a, 19-20, 22-23, 43b, 44] The higher temperature transition, α_{pc}, occurring at *ca.* 117 °C for the PFIA and *ca.* 170 °C for the PFSA, is associated with long-range motions of the backbone and the side chains that result from the weakening of the electrostatic interactions within the ionic aggregates.[5a, 19, 44] The higher temperature of α_{pc} for the PFSA with respect to PFIA is interpreted on the basis of the interactions between the side chains in the hydrophilic domains (see Scheme 1). Indeed, it is expected that owing to the higher flexibility of the side chains in PFIA, in accordance with Scheme 1, a distribution of solvated intra- and inter-side chain interactions characterize the hydrophilic domains of PFIA, which better delocalize the proton; this lowers the α_{pc} transition temperature. In contrast to the PFIA, the shorter, less flexible chain in the PFSA is expected to exhibit stronger inter-side chain interactions that increase the temperature of the α_{pc} event.

All of the above thermal transitions and changes are further confirmed through FT-IR studies (see Figure 3), where there are clear spectral differences between the respective hydrophobic domains of each membrane type. These differences highlight the differing helical conformations within the hydrophobic PTFE domains.

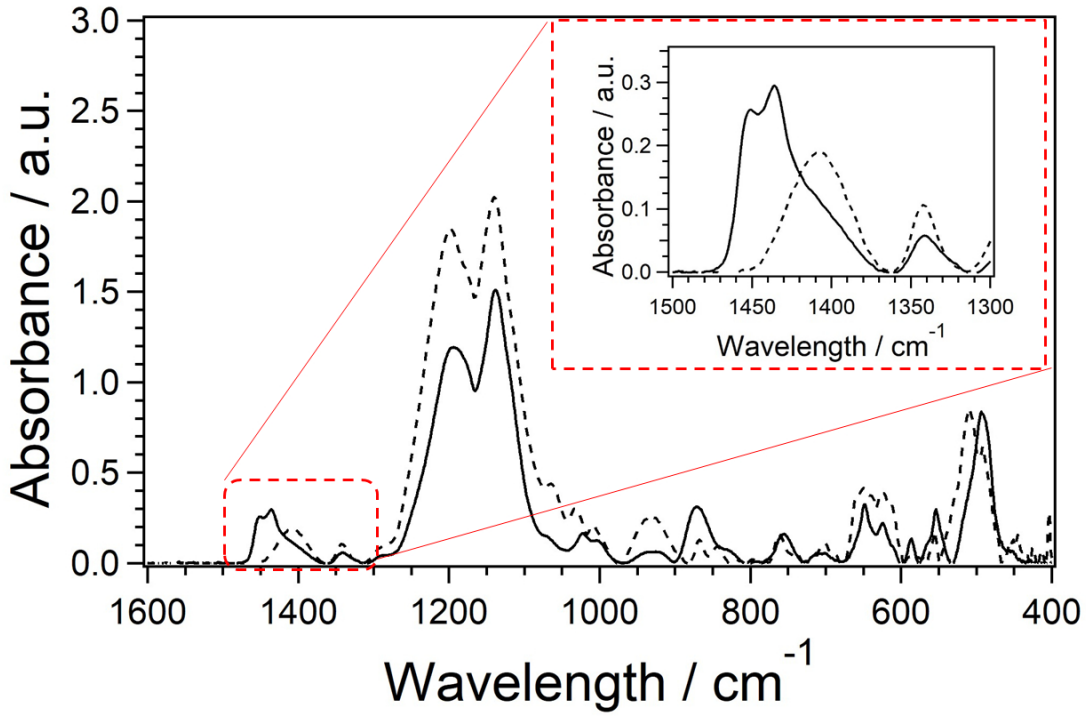

Figure 3. FT-IR ATR spectra of PFIA (solid line) and PFSA (dashed line) in their dry states in the region 1600-400 cm^{-1}. The inset magnifies the spectral region between 1500 and 1300 cm^{-1}.

For the PFSA, a band centered at 1408 cm^{-1} associated with ν(S-OH) and a band at 930 cm^{-1} associated with ν(C-SOOH) are observed. The spectrum of the PFIA exhibits a doublet, observed at 1450 and 1435 cm^{-1} in addition to the 1408 cm^{-1} band (see the inset of Figure 3). The two peaks of the doublet are observed in the dry form of the PFIA and are attributed to the terminal ν(S-OH) groups of the side chains.[5a, 10a, 19-20, 41, 45] These results confirm that, in dry conditions, the PFIA sulfonic-acid groups are clearly involved into two types of structural distributions modulated by intra- and inter-side chain interactions, respectively (see Scheme 1). It is expected that the stretching vibration at 1435 cm^{-1} is associated with the ν(S-OH) of the terminal sulfonic-acid groups of the looped side chains modulated by the intra-side chain interactions (see Scheme 1A). These modes resonate at higher energies than that of the PFSA inter-side chains. The vibration at 1450 cm^{-1} corresponds to the ν(S-OH) of the B inter-side chain interactions (see Scheme 1B), which are better stabilized in terms of interaction enthalpy, but

entropically less probable. Finally, the shoulder at 1408 cm^{-1} indicates that in the PFIA, a very small concentration of side chains are present that are interacting by means of R-SO_3H ⋯ HSO_3-R inter-side sulfonic (ISS) acid group interactions. In summary, for the PFIA, the concentration of intra- (A), inter-side chain (B), and ISS acid groups increases in the order A > B > ISS. This result is in agreement with the MD studies of the structure of PFSA and PFIA ionomers, which demonstrate that in the PFIA, 60% of the side chains are curved forming intra-chain rings, while the remaining 40% maintain their linear extended structure interacting with the neighboring side chains.[46] These results are also confirmed by: i) the band at 930 cm^{-1} that is assigned to the bending vibration of inter chain interacting –SO_3H groups,[47] thereby supporting that in the PFIA the fraction of inter-chain R-SO_3H ⋯ HSO_3-R bridges is negligible; and 2) the peak at 821 cm^{-1}, associated with the ν(C–S) stretching mode,[48] showing that the symmetry around –SO_2 groups is lost and the peak increases activity in IR, resulting in rising intensity. Finally, for the PFIA, the ν(NH) band at 3204 cm^{-1} is now observed (discussed in detail below).

The membrane nanostructure is also examined in the diffraction regime using SAXS and WAXS (Figure 4, Figure S1)**.** It is apparent from the figure that, in the dry state, the ionomer peak of the PFIA persists after drying the film at 120 °C while that of the PFSA disappears. The fact that the PFIA could preserve a more apparent phase-separation above 100 °C indicates that the strong acid/base interactions (shown in Scheme 1) stabilize the structural features of the hydrophilic domains and facilitate the degradation event II in the TGA profiles (see Figure 1a). From Figure 4b, both the PFSA and PFIA exhibit broad WAXS features that can be fit to two peaks at $q_a \sim 1.18$, and crystalline peaks at $q_c \sim 1.24$ $Å^{-1}$, corresponding to inter-planar distances of ~5.3 and 5 Å, respectively.[5a] Multiple crystalline peaks observed for the PFIA that can be assigned to the polymer's PTFE domains, which consist of a blend of chains with 2_1, 15_7, 10_5 and 4_1 helical conformations. The helical structure of a perfluorinated backbone chain can be described with the X_t notation, where X indicates the number of CF_2 units present in the

repeat unit, which are distributed in *t* turns of the helix along the chain axis z, Scheme 2 (b-II). In the PTFE domains with the 10_3, 15_7 and 4_1 conformations, we expect to have helices, while in the 2_1 domains the backbone CF_2 units are located in a plane with trans- (T) geometry (TTT) (see Scheme 2a). Helical conformations of crystalline domains can only be formed when a close-packing of the PTFE backbone chains is allowed. As previously demonstrated in other ionomers,[5a] close packing of the backbone chains depends on the IEC of the material and is possible only if the lateral groups are located in a linear direction that is parallel to the chain axis on the cylindrical-like surface of the helices (Scheme 2 (b-III)). The results reported in Table 1 indicate that the crystallinity of the PFIA is higher than that of the PFSA, which approximately agrees with the surface FT-IR ATR analysis carried out in the CF_2 region (see below). The same trend is also revealed for the fraction and size domains with a 2_1 conformational geometry; however, the opposite trend is observed for the size of 10_3 crystalline domains.

For the PFSA, this condition is achieved when the backbone chain assumes the 10_3 helical conformations, while the 15_7, which is the commonly preferred stable conformation for PTFE, corresponds to a helical chain that spreads the side chains statistically around the entire cylindrical surface defined by the helical geometry of the backbone (Scheme 2(b-I)). This is in accordance with other studies of the PFSA, where q_c and q_a are associated with the domain spacing of the backbone chains in the crystalline (with 10_3 helical conformation) and amorphous (with 15_7 geometries) PTFE domains, respectively. The peak at q_c ≈ 0.9 $Å^{-1}$ ($d \approx 7Å$) is very weak in the PFSA and corresponds to the interplanar distances of the crystalline domains with the 2_1 conformation. In this case, the carbons of the CF_2 backbone units are located in a plane and assume a TTT geometry. This backbone geometry allows the polymer chain to form crystalline lamellas by stacking these planes (see Scheme 2a). Figure 4b clearly shows that a larger fraction of q_c and $q_{c'}$ is observed in the PFIA, wherein the intra- and inter-side chain interactions between the side chains help modulate the morphology of the PTFE crystalline domains.

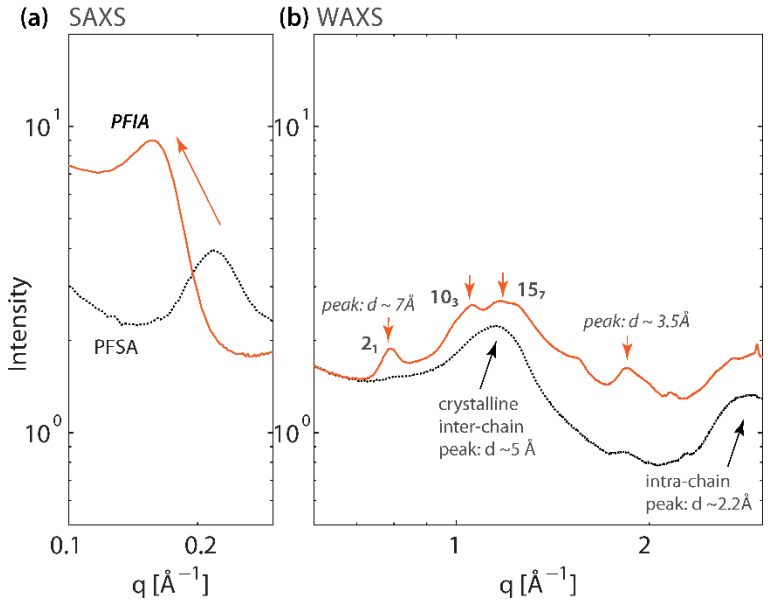

Figure 4. (a) SAXS and (b) WAXS profiles for dry 3M PFSA 825 EW membrane and dry PFIA membrane showing the characteristic diffraction peaks (marked with arrows).

Table 1. Relative degree of percent and size of crystalline and amorphous domains in PFSA and PFIA determined from WAXS.

	Conformation	q(Å^{-1})	% crystallinity	% amorphous	Size / nm
PFSA	2_1	0.86	0.8	-	2.8
	10_3	1.07	3.4	-	12.0
	15_7	1.18	-	30.3	4.5
PFIA	2_1	0.79	1.5	-	14.8
	10_3	1.03	9.4	-	7.1
	15_7	1.21	-	27.3	3.4

* Size of crystallite is determined by Scherrer formula.[49]

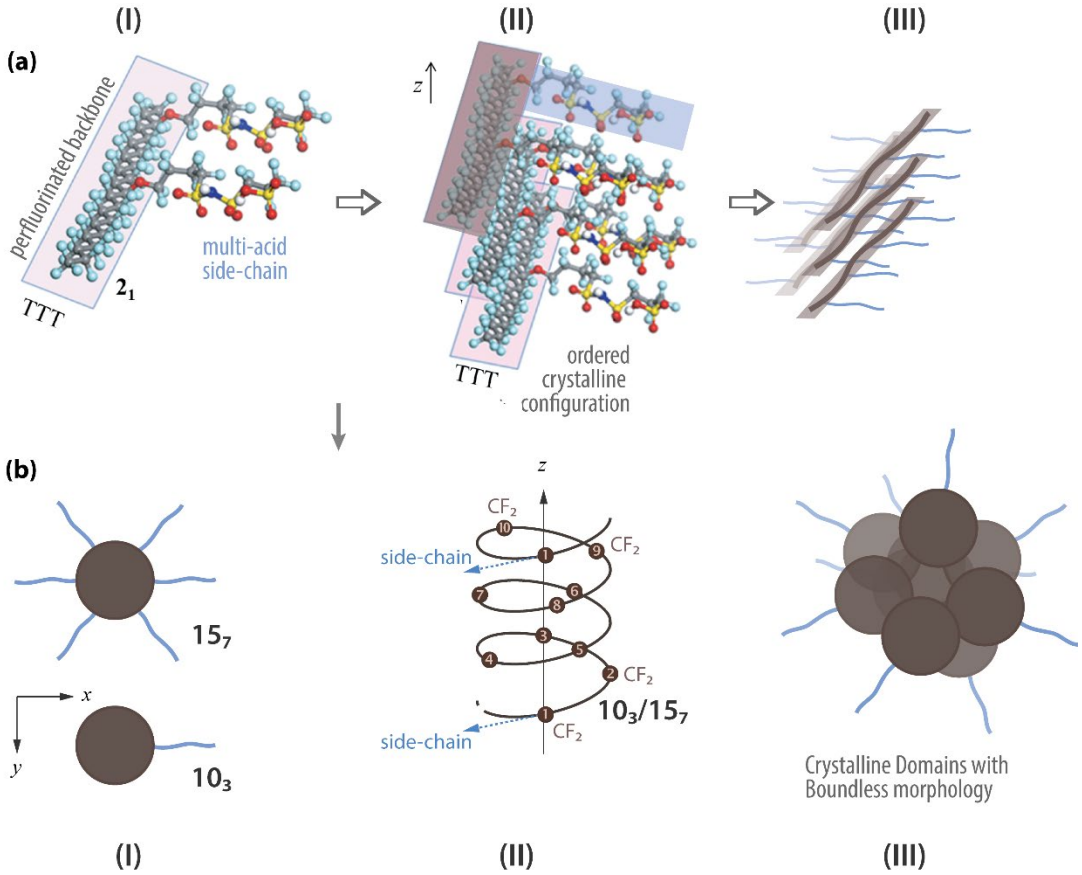

Scheme 2. Hypothetical representation of the proposed crystalline structure of the ionomer backbone. a) The 2_1 conformation leads to crystalline lamellae by stacking their planes (a-II and a-III); b) the 10_3 conformation (b-I, lower) leads to crystalline domains with a boundless morphology (b-III); instead, the 15_7 conformation (b-I, upper) spreads the side chains statistically around the entire cylindrical like-surface defined by the helical geometry of the backbone chain (b-II).

HYDRATION BEHAVIOR AND PHASE SEPARATION. The above section discussed the nanostructure and molecular structure of the dry materials. However, it is known that as these polymers become hydrated, their base nano-morphology undergoes a structural reorganization, which has been shown to be necessary for efficient, water-mediated proton conduction.[3a] As shown in Figure 5, the water uptake of the PFIA is greater than that of the PFSA, although the shapes of the curves are similar. Both membranes exhibit similar sorption behavior with the PFIA absorbing slightly higher water (*e.g.*, λ_{PFIA}

> λ_{PFSA} + 1) over the entire RH regime. The fact that the higher uptake of PFIA is a constant offset from as low as 10% RH to 100% RH suggests that the PFIA is likely to have additional ("residual") water molecules even in the dry state, which could be attributed to the primary solvation of the second protogenic group.

To investigate the underlying physics behind the higher water uptake and conductivity of PFIA, the radial distribution functions (RDFs) of water and classical protons to the protogenic groups in the side chains were computed from MD simulations for the various hydration levels, and are shown in Figure S2. At all hydration levels, both protogenic groups demonstrate a significant affinity towards the classical protons in the form of hydronium ions and water molecules. For the hydronium ions, both protogenic groups exhibit a high proton coordination number in the first solvation shell (3.4 H_2O/proton for imide and 3.7 H_2O/proton for sulfonic acid groups), hence explaining the higher water uptake of the PFIA membranes.

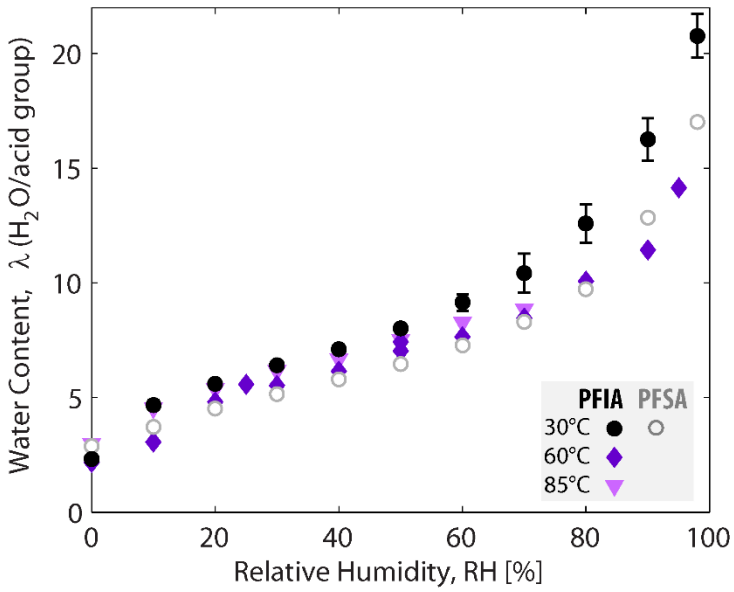

Figure 5. Water content per protogenic (acid) group for PFIA and PFSA membrane plotted as a function of RH at selected temperatures.

Furthermore, the sulfonic-acid groups at the ends of the side chains are significantly more attracted to both the protons and water than the imide groups in the middle of the side chains. This is inferred by the stronger peaks (larger amplitude) at around 4 Å for all hydration levels for both water and protons, as well as higher coordination numbers for these RDFs. These results suggest that the hydration process affects both ionomer regions in a similar way, with significant dilution of the protons occurring in the vicinity of both acid groups. Both protogenic groups have strong solvation shells, which result in additional water being retained around the imide groups of the side chains in addition to the water around the end sulfonic-acid groups.

A model of the PFIA polymer was developed to give further insight into the molecular dynamics (MD) of the hydrated polymer. More in-depth analysis from MD is provided by examining the Heterogeneity Order Parameter (HOP), defined and discussed in more detail in the SI and shown in Figure S3, where a higher HOP value is attained when the sites are closer to each other, indicating a closely packed or more clustered arrangement. As shown in Figure S2, the water molecules have a preference to cluster around the sulfonic-acid groups, hence causing an increase in their distance to acid groups with increasing hydration, thereby leading to a decrease in the HOP (lower degree of clustering). Conversely, for both the backbone atoms and ether groups on the side chains, the HOP values increased with hydration, which is attributed to water clustering near the side chain middle and ends. As the amount of water in the systems is increased, the water clusters around the end of the side chains and the hydrophobic backbone structure are forced to pack together, leading to a rise in the HOP value (higher degree of clustering), resulting in an enhanced hydrophobic/hydrophilic nanophase separation, especially at higher λ (15 to 20).

To further compare the local structure and water uptake of the PFIA and the PFSA, RDFs of the PFIA were compared to previously published RDFs for the PFSA by Tse *et. al.*[8a] They showed that reactive hydrated proton dynamics have a very small impact on RDFs and the corresponding coordination numbers for the PFSA and the longer side chain polymer, Nafion®. Hence, it can be concluded that the RDFs and coordination numbers presented in this work (Figure S5 and S6), although being from nonreactive simulations, are an accurate representation of the local interactions in PFIA. The results demonstrate that the protons are more attracted to the end sulfonic acid group in PFIA as compared to PFSA as shown in Figure S7 and S8.

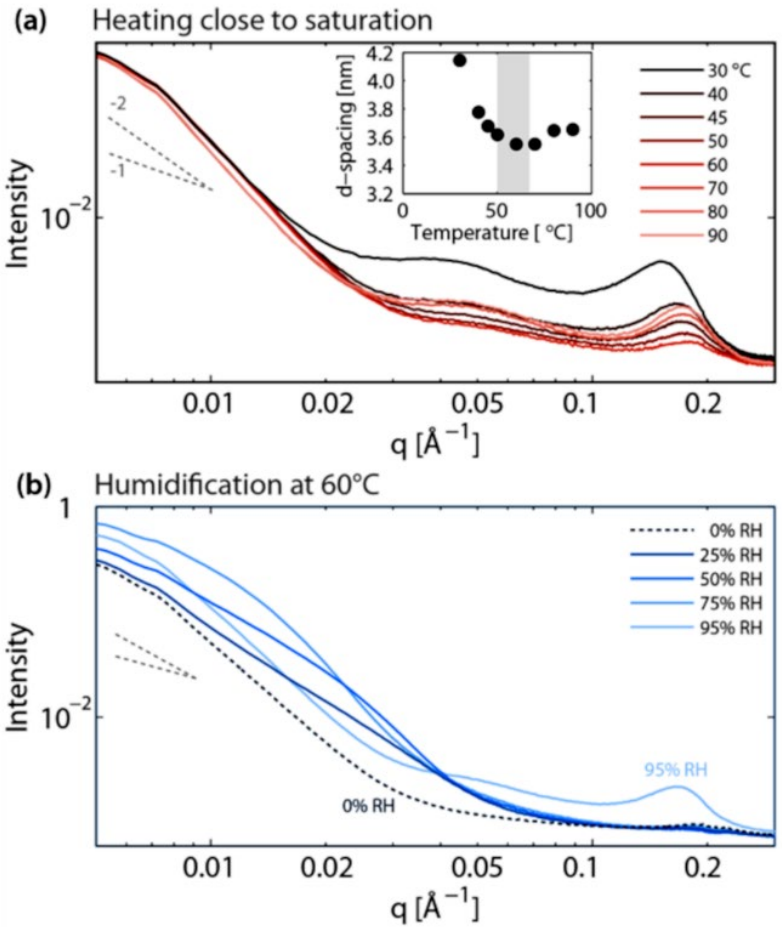

Figure 6. (a) SAXS profiles of PFIA membrane as a function of temperature at 95-98% RH. Inset shows the d-spacing of the ionomer peak as a function of temperature for the temperature sweep close to saturation. (b) SAXS profiles of PFIA membrane during humidification at 60 °C.

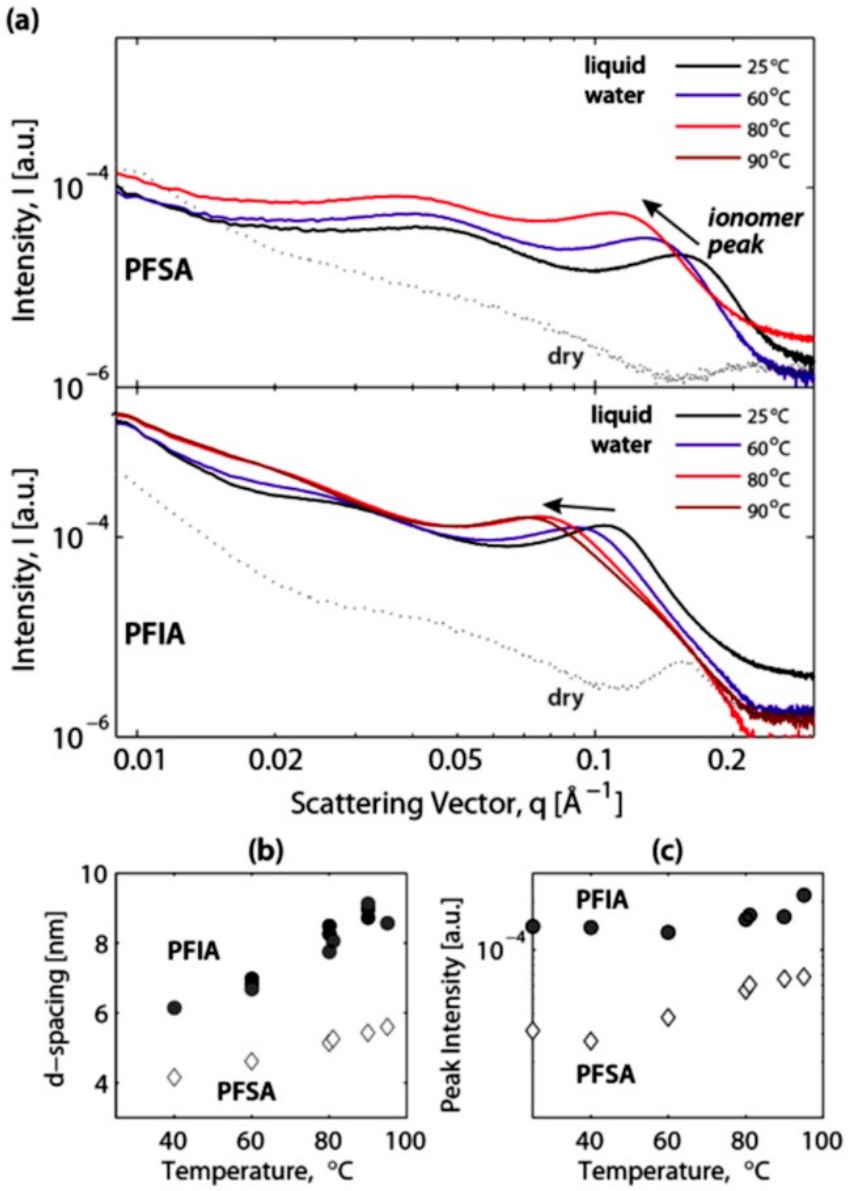

Figure 7. (a) SAXS profiles for 3M PFSA 825 EW membrane and PFIA membrane in liquid water at four temperatures. The profiles in dry conditions are also included for comparison. (b) d-spacing and (c) intensity of the ionomer peak as a function of temperature during heating in liquid water.

As expected for ionomers and from the MD simulations described above, a phase-separated morphology is anticipated with increasing hydration. To probe this, SAXS was performed under various temperatures in humid (Figure 6) and liquid (Figure 7) conditions. With increasing temperature, both ionomer peak

intensity and position shift in the saturated membrane. The d-spacing, corresponding to the correlation length of hydrophobic/hydrophilic regions, exhibits a non-monotonic dependence on temperature, with a transition around 60 °C (see the inset of Figure 6a). This trend differs from that for traditional PFSA materials.[42a] While the intensity of the ionomer peak decreases between 30 and 60 °C, the peak intensity starts to increase once again after 60°C. Similarly, the d-spacing decreases with temperature up to 60 °C and then exhibits a slight increase between 60 and 90 °C, see the inset of Figure 6a.

To investigate this transition further, SAXS patterns were collected using a humidity sweep at 60 °C (Figure 6b). The membrane was first allowed to equilibrate at 60°C and 0% RH, and then RH was increased sequentially up to 95%. The ionomer peak is rather broad and does not change up to 75% RH, indicating a lack of strong phase-separation. Once the humidification is increased from 75 to 95%, however, the ionomer peak becomes more pronounced revealing a morphological transition governed by the hydrophilic groups, or their growth with water uptake, in agreement with the MD simulations and thermal studies discussed above. The fact that a transition in the SAXS patterns is observed at 60 °C and 75% RH suggests an interplay between thermally-activated polymer-chain dynamics and water-mediated changes in the hydrophilic/hydrophobic phase-separation. There is an inflection point corresponding to a feature that is *ca.* 15 nm; this change is rapid and the SAXS data collection intervals (5 min) did not capture the dynamics occurring at much faster timescales, which is examined using BES as discussed later.

The nanostructure of the PFIA in liquid water also exhibits a strong temperature dependence, which, however, deviates from that observed for a PFSA membrane (Figure 7). Both the PFIA and PFSA exhibit a larger d-spacing with increasing temperature in liquid water. An interesting finding is that, while the peak intensity for PFSA increases with temperature, as does its d-spacing, the peak intensity of PFIA

demonstrates negligible temperature dependence (Figure 7b and Figure 7c). Such a behavior can be associated with a hydrated morphology that swells locally with heating (increase in d-spacing) but does not exhibit any strong structural organization in terms of its hydrophilic cluster distribution or network connectivity – thus the insensitivity of peak intensity to the temperature changes. Moreover, in liquid water, d-spacing of PFIA is 50% larger than that of PFSA, over the temperature range of 25 to 95 °C, which is probably related to the different interfacial reorientations that occur within the two materials, wherein the PFIA provides a lower energy for the water to enter and expand due to different swelling interactions compared to the PFSA.[3a, 50] At higher temperatures, the PFIA's d-spacing approaches almost 10 nm (*vs.* ~5 nm for the PFSA). This observation is consistent with the thermo-analytical results demonstrating that in the hydrophilic domain the interactions between side chains are of the type depicted in Scheme 1B, whose distance is approximately double of that determined by PFSA side chains inter-side chains interactions. It is expected in the PFIA that the increase of the fraction of bundle (10_3) and lamellar (2_1) crystalline domains tend to reduce the size of the amorphous PTFE domains, leading to a more effective packing of water clusters within less-disordered hydrophilic domains. Thus, the local structure and layering in the PFIA are interpreted as hydrophilic domains with larger separation distance (d-spacing), but comprised of smaller water clusters associated to each side chain interface within these domains. Such an interpretation is in accordance with the SAXS data, which shows that the interplanar d-spacing of the ionomer peak change only *ca*. 5 Å (see Figure 7) going from the PFSA ($d \approx 31$ Å) to the PFIA ($d \approx 36$ Å), despite the longer side chains in the PFIA.

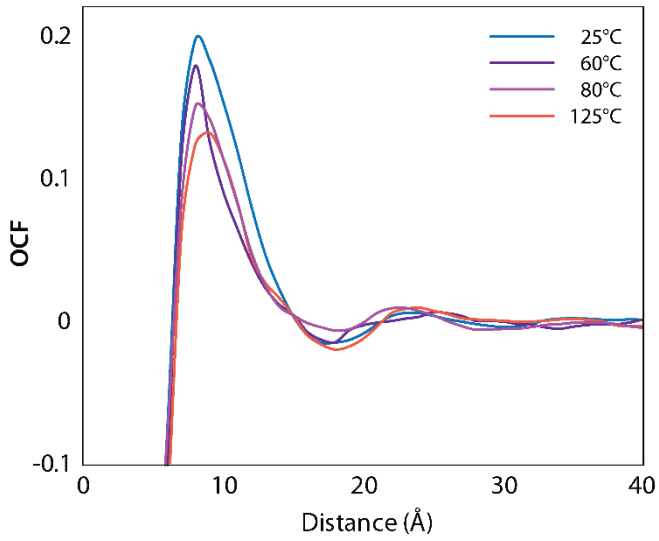

Figure 8. OCF for side chains for λ = 20 at 25˚C (red), 60˚C (blue), 80˚C (green) and 125˚C (black). Results for all other hydration levels studied are shown in Figure S8.

The above interpretation is also consistent with the MD simulations, where the Orientational Correlation Function (OCF) is shown in Figure 8 and Figures S9 and S10. The OCF is defined as

$$OCF(r) = \left\langle \frac{\left[3\left(\vec{u}(r_i)\cdot\vec{u}(r_j)\right)^2 - 1\right]}{2} \right\rangle \qquad (2)$$

where $u(r_i)$ is the unit vector as defined above for each of the side chains and backbone units (see Figure S11), and the correlation is averaged over all side-chain or backbone pairs as a function of distance between side chain or backbone pairs. The OCF ranges from 0, for completely uncorrelated orientations, to 1 for completely correlated chains (*i.e.* parallel or antiparallel orientation). From Figure 8, a strong peak was observed at ~10 Å. This implies that there is a very high local structural ordering in the side chains, such that they prefer to be parallel or antiparallel to each other. Furthermore, there are significant features observable at larger distances for all systems studied, indicating that there exists a long-range

order in the side chain orientations. It is also observed that there is no trend with a change in temperature for the λ = 1, 5, and 15 systems, which is consistent with experimental observations, wherein no significant change in morphology was observed in the membrane over the temperature range investigated. Also, similar to the experimental SAXS results, a clear trend emerges for the λ = 20 system with changing temperature. The height of the OCF peak decreases from 25 to 60 °C, followed by an increase in the peak height with a further increase in temperature. This trend is consistent with the SAXS data, wherein the PFIA went to a more disordered structure when the temperature was raised from 30 to 60 °C, and the ordering increased with a further increase in temperature. This observation is attributed to the corresponding change in the orientational alignment of the side chains in the λ = 20 system, leading to this transition at 60 °C, which is similar to that explained by Scheme 1-2 and correlated to the well-known order-disorder events of hydrophobic PTFE described elsewhere for the PFSA domains.[6a, 19, 22] The OCF for the backbone is included in Figure S10, and exhibits a similar trend to the side chain ordering, where the local ordering structure does not exhibit any change with temperature for low hydration states, and exhibits a similar nonlinear trend for the λ = 20 system. To probe the phase separation and water-cluster environment in more detail, vibrational analyses of the wet PFIA and PFSA membranes were conducted via FT-IR. The acid forms (where the sulfonic acid proton remains covalently bound) and ionic forms (where the sulfonic acid is dissociated) can be clearly distinguished upon hydrating the hydrophilic domains of the membranes. Detailed IR studies of both the PFIA and PFSA have already been conducted and full spectral assignments can be found elsewhere in the literature.[10a, 19, 21, 45a, 47, 51] Only those bands deemed most relevant to the argument of this paper are discussed below.

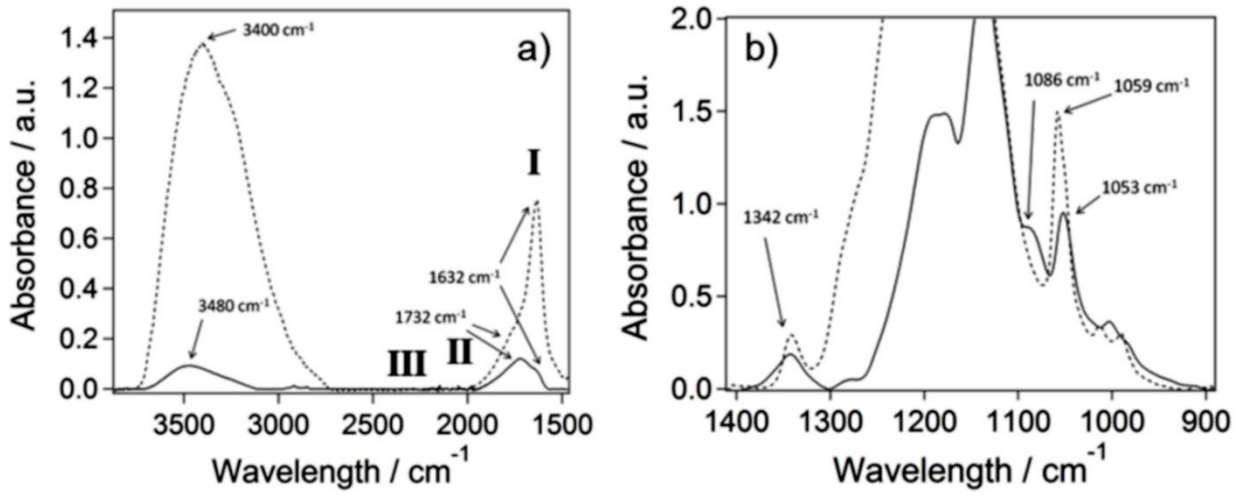

Figure 9. FT-IR ATR spectra of PFIA (solid line) and PFSA (dashed line) in their wet states in the regions (a) 1500-4000 cm^{-1} and (b) 900-1400 cm^{-1}.

For both the PFIA and PFSA membranes in their wet states, water-related absorbance bands dominate the respective spectra. However, there are noticeable differences in these water-based regions of the spectra between the two materials (see Figure 9). The intensity of the water-based bands is significantly higher for PFSA with respect to those of PFIA, indicating the presence of larger water clusters for PFSA in agreement with the various other data. The larger size of water clusters wetting the PFSA hydrophilic domains is the consequence of the structural reorganization of polymer chains into PTFE crystalline (10_3) and amorphous domains (15_7), which in turn results in more free space within the hydrophilic domains, in contrast to that occurs in the PFIA, and in agreement with the discussion above. Thus, despite the water-uptake increases in PFIA compared to PFSA (see Figure 5), the nature of the imbibed water in the two membranes is different. Indeed, in the PFIA a significant number of lamellar domains with 2_1 helical backbone conformations are present. The intense broader band centered at 3400 cm^{-1} for the PFSA is indicative of the stretching modes of bulk water, suggesting the presence of larger water clusters. This band is less intense and shifted to 3480 cm^{-1} for the PFIA, indicative of a less extended 3D hydrogen-bonded environment due to smaller water clusters solvating the side groups, which are also more

uniformly distributed along the polymer/water interfaces[19, 21, 48, 51b] particularly in the polymer domains with 2_1 geometries; a similar effect is observed in the region associated with the bending modes of water. The PFSA exhibits a strong band centered at 1632 cm^{-1} (I) with a shoulder at 1732 cm^{-1} (II). The PFIA exhibits complementary behavior with the 1732 cm^{-1} band (II) dominating and the 1632 cm^{-1} band (I) present as the shoulder. The higher intensity 1632 cm^{-1} band in PFSA again suggests the presence of larger water clusters ($[(H_2O)_n]$), where the water molecules behavior is similar to that of bulk water.[5a, 6a, 19, 48, 51b] The lower intensity of this band in the spectrum of PFIA suggests that the $[(H_2O)_n]$ water clusters are smaller in size in this membrane. Indeed, for the PFIA, the dominant band in this region is centered at 1732 cm^{-1} and is attributed to the presence of clusters of *"acid water"* ($\delta[H_3O^+ \cdots (H_2O)_n]$), where the H^+ is exchanged very fast between the water molecules, improving proton delocalization and transport. It has been previously observed that dehydrating a fully water-saturated PFIA membrane results in first, the loss of the *"bulk water"* band at 1632 cm^{-1}, followed by that of the *"solvation-shell"* band at very low hydration and much higher temperatures.[19, 28, 43b, 45a] It should be observed that for the PFSA and PFIA, no peak III associated with the $\delta([H_3O^+ \cdots SO_3^-]\cdot(H_2O)_n)$ mode is observed at $\nu > 1750$ cm^{-1}. III is attributed to the bending modes of water molecules solvating oxonium ion clusters directly interacting with the $R - SO_3^-$ anion groups.[6a, 48, 51b] This result indicates that the protons in the water domains are delocalized increasingly in the order PFIA >> PFSA, which will have an impact on the conductivity as discussed in the next section. In the wet state, the sulfonic-acid groups of the side group termini of both membranes are in the ionic state, which is to say that they are deprotonated.[5a, 19-20, 45b, 47] This gives rise to a variety of diagnostic peaks for both PFIA and PFSA membranes. For the PFSA, bands at 1342 cm^{-1} and 1059 cm^{-1} are observed and assigned to $\nu_{sym}(SO_3^-)$ and $\nu_{asym}(SO_3^-)$ bands. The spectrum of the PFIA also exhibits the 1342 cm^{-1} band of the $\nu_{sym}(SO_3^-)$ group, however, the band associated with the $\nu_{asym}(SO_3^-)$ is broader in nature and slightly shifted to 1053 cm^{-1} with respect to that observed for PFSA. This is a result of the smaller water clusters formed in the PFIA that gives rise to solvation shells as opposed to

the larger water clusters present in the PFSA. A third peak is observed at 1086 cm^{-1} that is present only in the spectrum of the PFIA and is assigned to the ν_{sym} (SO_2) of the sulfonyl imide.[45a] Finally, care must be taken when interpreting the two strong doublets (centered at *ca.* 1188 and 1138 cm^{-1}) that are present in the CF region of the spectra for both the PFIA and PFSA. In this region, there are contributions arising from the CF_2 modes of various different helical conformations of the fluorocarbon backbone chains in the PTFE domains.[5a, 19, 47, 52] There may also be contributions from COC, SO_2, and SNS modes,[10a, 45, 47, 52g] however, based on the stoichiometry of the membranes, these are likely to be minor contributions and so in accordance with other studies;[51b] this region is dominated by the vibrational modes diagnostic of the type of different helical conformations of PTFE backbone chains. Figure 10 clearly shows that the hydrophobic domains of both the PFSA and PFIA are based on a blend of perfluorinated backbone chains with different conformations. This result agrees with other studies[51b, 52a, b] and the WAXS results (Figure 4). There is a clear difference between the PFIA and PFSA in terms of the weighted contributions of the 15_7, 10_3 and 2_1 helical conformations. It is evident that the peaks corresponding to the 10_3 and 15_7 are dominant for PFSA with respect to the 2_1 geometries. Therefore, on the basis of the peak assignment reported in Figure 10, we can summarize that the hydrophobic PTFE domains of PFSA and PFIA are comprised of a blend of helical chains with the conformational fraction decreasing in the order $10_3 > 2_1$; the fraction of 2_1 chains, which are negligible in the PFSA, is significant in the PFIA; and going from the PFSA to PFIA raises the fraction of 10_3 and 2_1 crystalline domains and decreases the abundance of 15_7 amorphous domain.

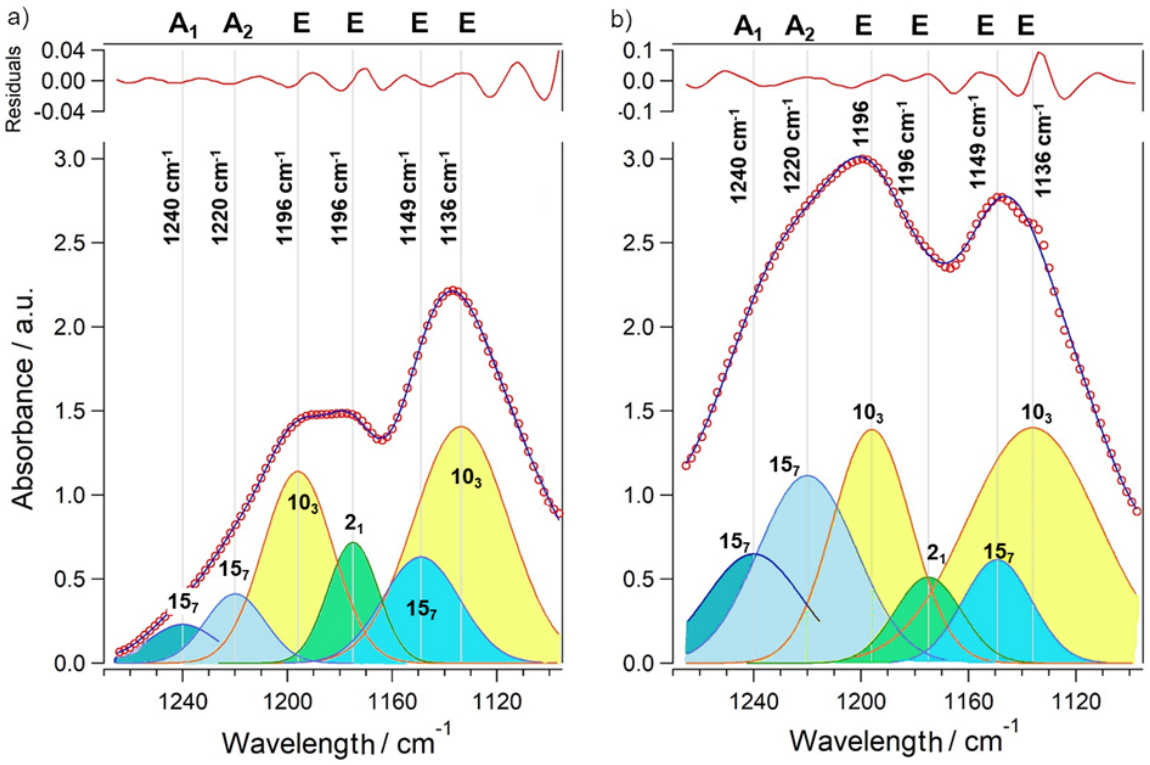

Figure 10. FT-IR-ATR of wet PFIA (left panel) and wet PFSA (right line) in the CF_2 region 1100-1260 cm^{-1} The assignments summarized in the figure were performed correlatively on the basis of previous results on perfluorinated backbone chains with different conformations (10_3, 15_7, 2_1 and 4_1). In order to better support the correlative assignment of the vibrational modes shown in the figure, the spectral profiles of PFIA and PFSA were decomposed by Gaussian functions as elsewhere described.[51b, 52a, b, 53]

Overall, the hydrated nanostructure exhibits significant differences between the PFIA and PFSA, where the various inter- and intra-side chain interactions modulate the composition and hence the water clustering and domain alignments. A higher concentration of the 2_1 conformation in the PFIA increases the density of lamellar morphologies, which act to absorb water at their existing interstices and interfaces. This reduces the size of water clusters, enhances their distribution and increases the local water uptake (per acid group), which agrees with the larger spacing of hydrated domains in PFIA (Figure 7). These interactions are temperature dependent and dictate the overall nanostructural rearrangement with

hydration. Furthermore, the presence of a predominating concentration of side chains of type A (Scheme 1), whose structure is modulated by intra-side chain interactions, improves the delocalization of protons in the solvation water *"shells"* present at the interstices of PFIA hydrophilic domains. This delocalization is thus expected to impact the proton conductivity of the membranes, especially under intermediate hydration conditions where the differences are most extreme.

PROTON CONDUCTIVITY. The above sections detail the hydrated environment and especially the nanostructure and underlying structure/function relationship of hydration, but do not discuss the transport phenomena that are engendered. In this section, the protonic conductivity of the PFIA is examined and compared to the PFSA to elucidate how the local water environments and nanostructure impact proton conduction. The through-plane conductivity of the PFIA membrane as a function of RH is summarized in Figure 11. At 30 °C, the PFIA clearly exhibits higher conductivity than the PFSA at lower RH, *e.g.*, ~ 0.03 *vs.* 0.01 S/cm at 40% RH for the PFIA and PFSA, respectively. With increasing humidity, however, the relative difference between their conductivity diminishes from 200% down to 20% at 98% RH. PFIA has superior conductivity at all intermediate RH conditions, which is due to the role played by the multiple acid groups in the PFIA side chain. The positive impact of the multi-acid chain on conductivity manifests itself even more strongly at the higher temperatures measured, 60 and 85°C. Here, there is a change in shape of the curves for the PFIA to almost linear with RH (as opposed to the more concave shape of a typical PFSA), where the middle region (40 to 80% RH) is more sensitive to the side chain chemistry. As with the low temperatures, the conductivities of two membranes get closer as they approach 100% RH.

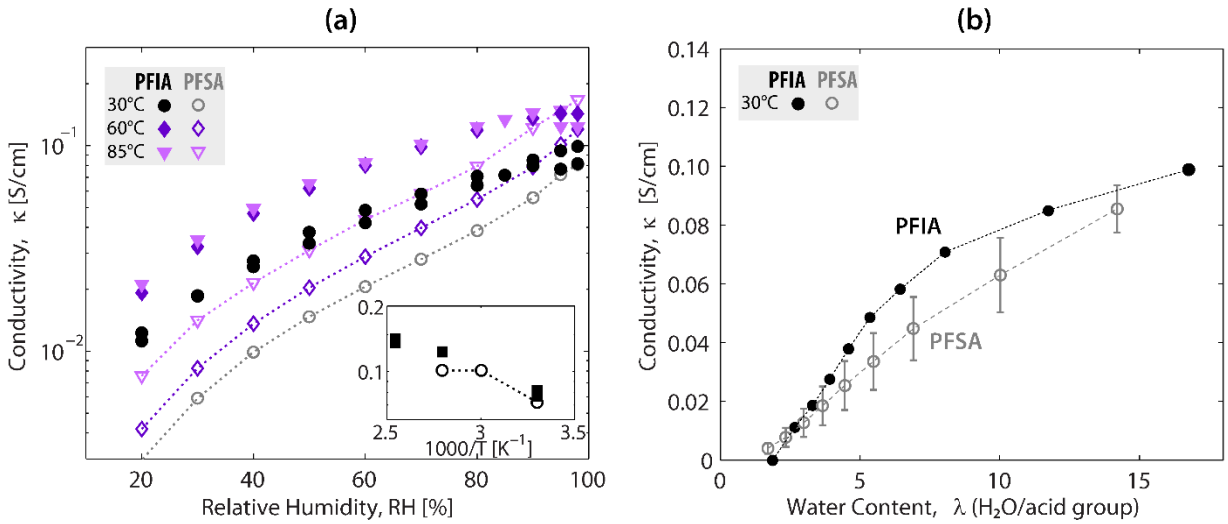

Figure 11. (a) Through-plane proton conductivity of PFIA and PFSA membrane as a function of RH at three temperatures shown in log scale, where the inset shows the Arrhenius plot at 60 and 90% RH. (b) Conductivity (from a) *vs.* water content (from Figure 5) at 30 °C for the two membranes.

To understand this trend better, the conductivity is plotted as a function of water content, λ (water molecules per acid group) in Figure 11(b), which shows that even at the same λ, the PFIA has slightly higher conductivity than the PFSA. Nevertheless, the conductivity values converge at maximum λ (close to saturation). Thus, it is to be expected that the charge carrier density in both the PFSA and the PFIA are almost the same and that the difference in the conductivity is simply associated to a change of proton mobility in the two different structural environments, specifically in the hydrophilic domains of the bulk PFSA and PFIA membranes. This evidence is in contraposition with the assumptions performed for PFIA elsewhere.[46] This experimental evidence can be quantitatively rationalized by considering that the dissociation constants of the two different chemical functionalities characterizing the PFIA side chains cannot be equal. Furthermore, the shape of the curves in Figure 11(b) also overlap substantially and thus do not appear to be a superposition as expected for similar dissociation; please see the SI for a more detailed discussion. The higher conductivity for the PFIA compared to the PFSA at the same humidity

occurs as well for the in-plane conductivity (see experimental in SI and data shown in Figure S12). Both polymers demonstrate an anisotropy in conductivity, which may be due to the measurement technique since the through-plane measurement has a more complicated setup and involves possible influences due to the interfacial phenomena including perhaps the impact of surface layers, as has been described previously for PFSA membranes.[51a, 54] The differences in conductivity can be rationalized by the different hydrated nanostructures discussed above. At drier conditions, the PFIA's multi-acid side chain lends itself to smaller water clusters, associated directly with the side chain movements and interactions. Such an orientation also enables a more efficient hopping mechanism for proton conduction, even at minimal water contents.

To further investigate the conductivity, self-diffusion coefficients of water and the hydronium ions (H_3O^+) in the PFIA membranes were computed theoretically and compared to diffusion coefficients determined from pulse-field gradient spin echo NMR (see Figure S13). The diffusion coefficients calculated from the mean squared displacements (MSD) of all water and hydronium hydrogens in the NVE ensemble demonstrated good agreement with experiments for the hydrated PFIA (95% RH, λ = 20). The calculated diffusion coefficients for the hydrated PFIA (95% RH, $\lambda = 20$) demonstrated excellent agreement with experiments with an Arrhenius-type temperature dependence. This agrees with the *ab-inito* MD studies by Clark and Paddison[8i] showing that the first proton dissociation occurs in PFIA at a lower λ (than that in PFSA), due in part to the direct hydrogen bonding between the acid groups. In such a scenario, one would not only expect higher water content (λ) at the same RH and higher conductivity at the same λ, but also a change in the shape of the conductivity-RH (or κ-λ) curve (see Figure 11). As more water is added to the ionomer, such transitions become similar for the different side chains as conduction is now more hydration dependent, where the protons are more dissociated and transport occurs in the further hydration shells in agreement with the MD simulations. As the polymers enter a

very dry state, however, this movement is arrested and the protons become more tightly bound to the first hydration shell, resulting in similar conductivity for PFSA *vs.* PFIA. It is noteworthy that the PFIA side chain moiety and structure plays a critical role in pushing/keeping the hopping-type transport down to lower humidities. An important consideration while comparing experimental diffusion coefficients of wet PFIA and PFSA membranes is that since experimentally there is no distinction between the excess protons and the hydrogens belonging to the water molecules, the final measured value is expected to be similar to the diffusion coefficient of water in these systems at least at very high water contents. Using MD, we distinguish the hydronium ions from water, which enables comparison of diffusion processes from nonreactive simulations, as shown in Figure S14. Compared to the PFSA, the diffusion coefficient is higher in the PFIA for both water and hydronium, although the latter increases more as the hydration level is increased, regardless of temperature, which indicates a higher contribution to proton diffusion from charge exchange processes between different coordination sites in the PFIA membrane.[8a]

CONDUCTION MECHANISMS AS DETERMINED BY BES

The above discussion details the PFIA macroscopic conductivity, Figure 11, as a function of hydration and how it can be related to its hydrated nanostructure. However, to explore the conduction mechanism in more detail and demonstrate definitive structure/function interplay, the electric response and relaxation events of the PFSA and PFIA membranes in both wet and dry conditions are investigated and compared by Broadband Electric Spectroscopy (BES) in the range of −140 to 150 °C and 0.03 to 10^7 Hz. It should be noted, as discussed above, the two PFIA acid moieties, *i.e.,* the terminal sulfonic acid group and the sulfonimide group in the middle of the side chains (Figure 1b), are not expected to be equally dissociated. From the conductivity and characterization analysis above, it appears that the super acid R-SO_3H terminal group dissociates first and inhibits the dissociation of the sulfonamide group in PFIA membrane due to

the inter-side chain interactions. In the interest of brevity, the most important points of the data set are espoused below; additional important data and thorough discussion are in the SI.

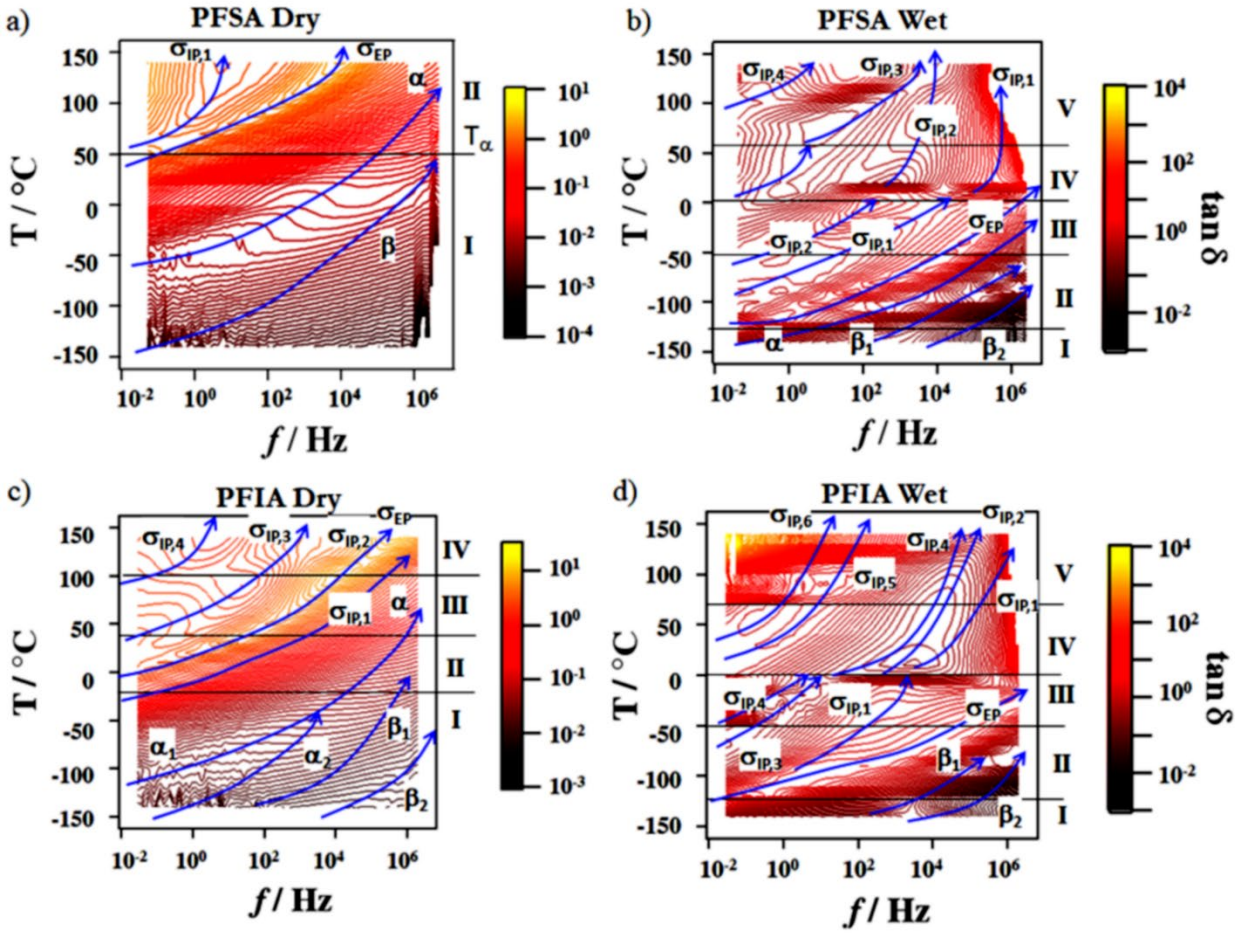

Figure 12. Contour plot of tanδ for PFSA (a, b) and PFIA (c, d) membranes in dry (a, c) and wet (liquid) (b, d) conditions.

From the BES, the tanδ = ε''/ε' surface represented as a contour plot (Figure 12) is particularly useful in identifying the relaxation events present in the PFSA and the PFIA membranes and the effect of the thermal transitions on the electrical response of the materials.[55] In dry and wet PFSA and PFIA, tanδ (Figure 12) shows:

1) for the dry PFIA, three dielectric relaxations (α, β_1 and β_2) and five polarization events, both electrode polarization (EP) and interdomain polarization (IP) (σ_{EP} and $\sigma_{IP,i}$ with $1 \leq i \leq 4$). At T

< -50 °C, α is split to α_1 and α_2. For the dry PFSA two dielectric relaxations (α, β) and two polarization phenomena (σ_{EP} and $\sigma_{IP,1}$) are observed;

2) for the wet PFIA, two dielectric relaxations (β_1 and β_2) and seven polarization events (σ_{EP} and $\sigma_{IP,i}$ with $1 \leq i \leq 6$). For wet PFSA, three dielectric relaxations (α, β_1 and β_2) and five polarization phenomena (σ_{EP} and $\sigma_{IP,i}$ with $1 \leq i \leq 4$).
3) the dry PFSA presents only one IP which in wet conditions is split into 4 IPs, while b) the dry PFIA presents 4 IPs which in wet conditions are split into 6 IPs.

The σ_{EP} is assigned to the electrode polarization, which is due to an accumulation of charge at the membrane/electrode interface,[55-56] while $\sigma_{IP,i}$ is associated with an interdomain polarization phenomenon[55-56] due to the presence of inhomogeneities within the bulk material, which correspond to the accumulation of charge at interfaces between domains with different permittivity. These results confirm the structural and spectroscopic results discussed above. Indeed, the hydrophobic domains of the PFSA consist mostly of a blend of 10_3 and 15_7 conformational chains, and the hydrophilic domains are composed of a very simple side chain. A more complicated situation is expected for PFIA, where different types of side chain rearrangements are possible (see Scheme 1) owing to both the intra and inter-side chain interactions, and there are three types of conformational geometries for the perfluorinated chains (10_3, 2_1 and 15_7) in the hydrophobic domains. These structural scenarios easily account for the increase in the number of IPs from 1 to 4 (PFSA) and from 4 to 6 (PFIA) in the dry and wet membranes, respectively.

The dry PFSA and PFIA present 2 (α and β) and 3 (α, β_1 and β_2) dielectric relaxations (see Figure 12a and Figure 12c). α, in accordance with other studies,[5a, 6a, 20, 22, 41, 52e] is assigned to the diffusion processes of conformational states along the perfluorinated backbone chains (segmental motions). This mode at T

< –50 °C for the PFIA is split into a doublet, thus indicating that two different ordered PTFE domains are present at low temperatures in the PFIA. This evidence is consistent with the vibrational and X-ray studies described above,[51b, 52a, b] which showed that in the PFIA at low temperature the PTFE chains tend to reorganize into hydrophobic crystalline domains with the polymer backbone chains in both the 10_3 and 2_1 helical conformations (see Table 1). At T > 10°C, α_1 and α_2 merge together forming the α relaxation. This indicates that the segmental motions of the perfluorinated backbone chains, with different conformations, become indistinguishable. The PFSA β relaxation is attributed to the fluctuation of the dipole moment of the side groups. In dry PFSI, two β-relaxations are detected: β_1 and β_2. β_1, which occurs at low frequencies and is the most hindered dipole moment fluctuation, is attributed to the dipole fluctuations of straight side chains (B interaction of Scheme 1). β_2 is associated to the relaxation mode of dipole moment of the curved side chains (see A model of Scheme 1), as expected the intra-chain interactions are weaker with respect to inter-side chain interactions. Thus, the rate of relaxation of β_2 is higher than that of β_1. In wet conditions, the presence of water modulates the structural reorganization of the side chains, thus affecting the distribution of the 10_3 or 15_7 backbone conformations. Thus, water triggers a distribution of PTFE backbone chain conformations in the hydrophobic domains increasing the number of the different PTFE hydrophobic domains in terms of their size and helical blend composition giving rise to different hydrophobic domains that split the IPs into 4 and 6 different events for the PFSA and PFIA, respectively. To examine this in more detail, the profiles of the real and imaginary components of the permittivity ($\varepsilon'(\omega)$) *vs.* frequency of the membranes are investigated (see Figure S15 and Figure S16). The results demonstrate that in the PFSA, the undissociated short side chains contribute less to the interdomain and electrode polarization phenomena; and in the PFIA, the presence of two groups with different dissociation constants allows the stronger R-SO_3H group to interact by means of intra- or inter-side chain interactions with the less strong sulfonimide group dissociating trace amounts of protons, which are thus delocalized and accumulate at the interfaces between domains of

differing permittivity. Such findings are in agreement with the thermal, X-ray and vibrational studies discussed above, confirming the presence of a significant fraction of PTFE lamellar backbone chains with the 2_1 conformational geometry in the PFIA, which increases the concentration of the hydrophobic domains with small sizes (and the larger domains with increased electron density), thus increasing the water uptake and reducing the size of water clusters. Thus, the water clusters embedded in the hydrophilic domains of the PFIA are smaller and better distributed with respect to those of the PFSA despite the water uptake of the latter membrane being lower. Figure 13 shows the spectra of the real component of the conductivity ($\sigma'(\omega)$) (for the sake of completeness -$\sigma''(\omega)$ is shown in Figure S17). It is observed that, in the dry membranes, the plateaus that correspond to the polarization events are correlated to the conductivity values of the charge migration pathways associated to these phenomena in PFSA,[19, 55-56] which are at least two orders of magnitude lower than that of the PFIA, in agreement with highly localized proton dissociation in dry PFIA (see Scheme 1). With respect to the PFSA, the relaxation rate of the PFIA from the EP behavior is shifted to high frequencies despite the plateau exhibiting conductivity values of the same order of magnitude. This proves that the concentration of charge carriers in the hydrophilic domains is the same in both membranes, but, the mobility of the protons in the PFIA is higher than that of the PFSA. This phenomenon can also be associated with the presence in the PFIA of a higher density of functional groups able to exchange protons, that include both the $–SO_3^-$ and imide acids. Such groups can more easily form diffusion pathways where protons can migrate easily without the need to move deep into the hydrophilic domains, in accordance with the interpretation provided by Savage *et al.*[57] Thus, in the PFIA, the intra- and inter-side chain interactions act to reduce the size of the water domains and increase the proton delocalization, thereby improving the effective proton mobility.

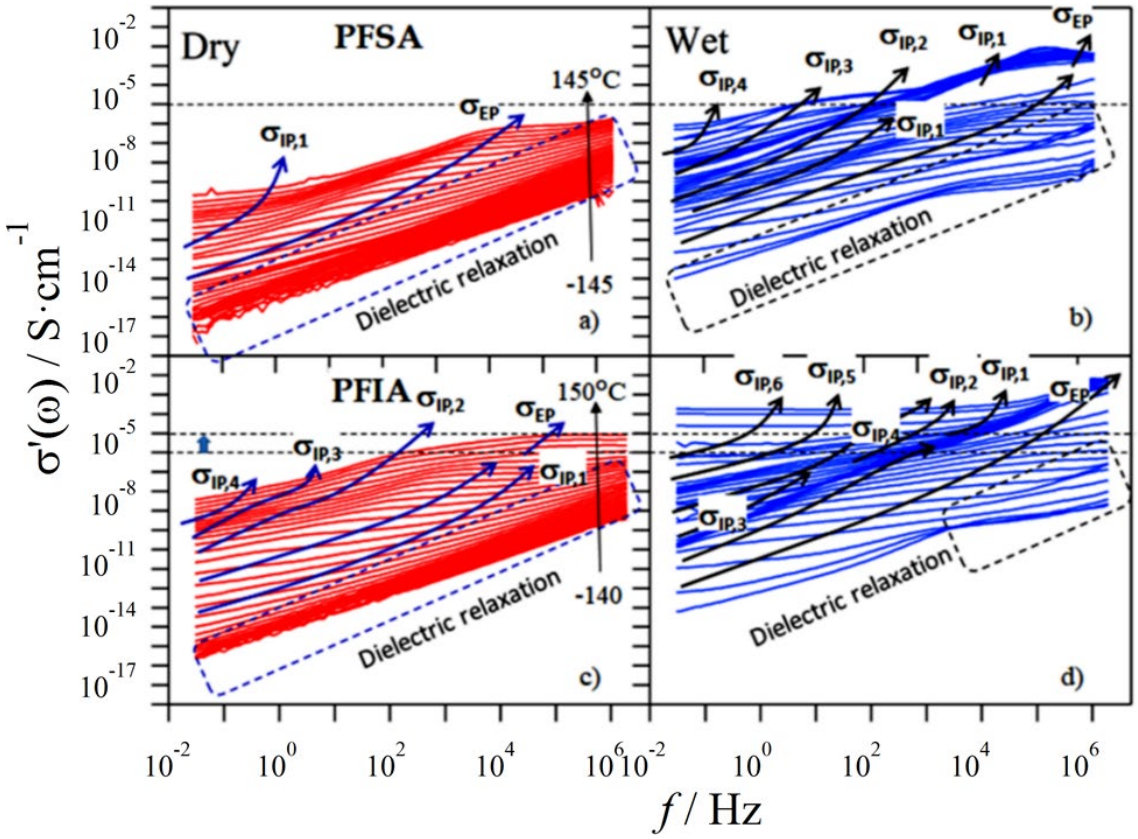

Figure 13. 2D of real component of conductivity (σ'(ω)) for PFSA (a, b) and PFIA (c, d) membranes in dry (a, c) and wet (b, d) conditions.

To study the relaxation events in detail characterizing the electric response of the PFSA and PFIA membranes and to elucidate their conductivity mechanism, the conductivity values and relaxation times attributed to the polarization phenomena and the dielectric strengths and relaxation times of dielectric modes are determined by fitting simultaneously all of the experimental profiles of ε'(ω), σ'(ω) and tanδ(ω) using:[56]

$$\varepsilon^*(\omega) = -i\left(\frac{\sigma_0}{\omega\varepsilon_0}\right) + \sum_{j=1}^{3}\frac{\sigma_j(i\omega\tau_j)^{\gamma_j}}{i\omega\varepsilon_0\left[1+(i\omega\tau_j)^{\gamma_j}\right]} + \sum_{k=1}^{4}\frac{\Delta\varepsilon_k}{[1+(i\omega\tau_k)^{a_k}]^{b_k}} + \varepsilon_\infty \qquad (3)$$

where σ_0 is the background conductivity, ε_0 is the permittivity of the vacuum, σ_j and τ_j are the conductivity and relaxation time associated with the j^{th} polarization event, while γ_j is its shape parameter that describes the broadness of the j^{th} peak. $\omega = 2\pi f$ is the angular frequency of the electric field. τ_k is the relaxation time ($\tau_k = 1/(2\pi f_k)$, with f_k is the frequency of the *k*-th dielectric relaxation events) of the k^{th} event of dielectric strength $\Delta\varepsilon_k$, and a_k and b_k are the symmetric and asymmetric shape parameters of the *k-th* dielectric relaxation mode. The last term corresponds to the instantaneous permittivity, $\varepsilon_\infty = \lim_{\omega\to\infty}\varepsilon'(\omega)$. Figure 14 shows the conductivity values as a function of inverse temperature. The effect of temperature on the ratio of conductivity ϕ_I and dielectric strengths is reported on Figure S18 and Figure S19, respectively. From Figure 14 it is possible to observe the presence of a maximum of: a) four regions (I, II, III and IV) in the dry membranes, which are delimited by their thermal transitions; and b) five regions (I - V) in the wet samples, delimited by the melting point of water, T_m (0°C), and the temperatures of –100, –50 and 60°C. The dry PFSA membrane in all regions (I and II) shows an overall conductivity, $\sigma_T = \sigma_{EP} + \sum_{i=1}^{6n} \sigma_{IP,i}$ (see Figure 14b and S17b), which is mostly associated to that of the electrode polarization event ($\sigma_T \approx \sigma_{EP}$ and $\phi_{EP} = \sigma_{EP}/\sigma_T \approx 1$ in Figure S18). In this case, the dependence of σ_{EP} on 1/T shows a Vogel-Tamman-Fulcher (VTF)[56] dependence that indicates that the σ_{EP} is facilitated by the dynamics of the polymer backbone chains, the segmental motions associated with the α relaxation. The dry PFIA shows a very different scenario (see Figure 14a and Figure S18a); in the regions I and II, $\sigma_T \approx \sigma_{IP,1}$ (Figure 14c) and $\phi_{IP,1} = \sigma_{IP,1}/\sigma_T \approx 1$ (Figure S18).

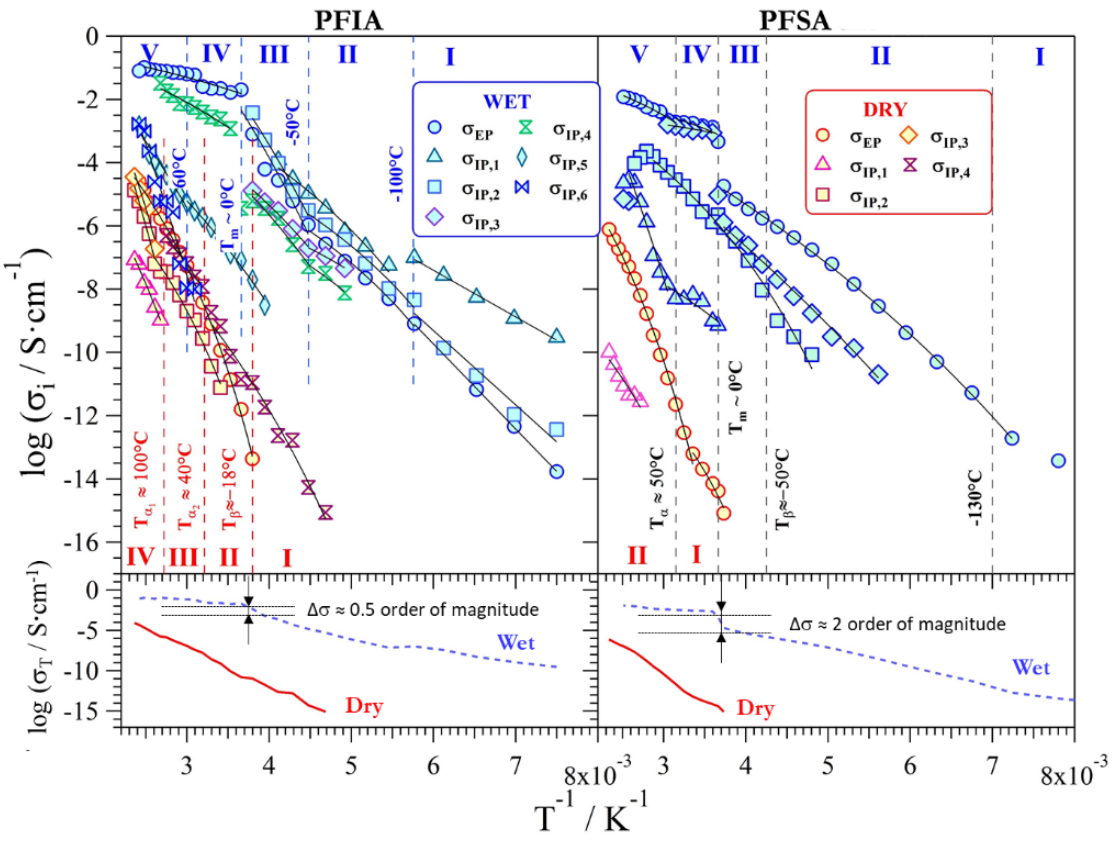

Figure 14. Conductivity σ_i ($\sigma_i = \sigma_{EP}$, $\sigma_{IP,I}$ with i = 1 to 6) values vs the inverse of temperature for PFIA (a) and PFSA (b) in dry and wet conditions. σ_i vs 1/T curves of dry and wet are fitted by Arrhenius-like or VTF-like behavior, respectively. In c) and d) the total conductivity ($\boldsymbol{\sigma_T = \sigma_{EP} + \Sigma_{i=1}^{6} \sigma_{IP,i}}$) for dry and wet of PFIA and PFSA, respectively, are reported.

These findings indicate that in these latter regions, the overall conductivity (which for the PFIA is higher than that of the PFSA) is due to long-range proton-migration events occurring at the interfaces between domains with different permittivity mediated by the segmental motions of the backbone chains. Indeed, in this case, the segmental motions of the PTFE chains are likely highly coupled with the dynamics of the interacting side chains. In this case, a VTF dependence of σ_{IP} is observed and a significant proton delocalization at the interfaces between hydrophobic and hydrophilic domains is expected. In regions II

and III, the analysis of Figure 14a and Figure S17a indicates that both σ_{EP} and $\sigma_{IP,1}$ are contributing (with $\phi_{EP} \approx \phi_{IP,1} \approx 0.5$) to the overall conductivity of the material ($\sigma_T \approx \sigma_{EP} + \sigma_{IP,1}$). This suggests that after 40 °C the segmental motions of the polymer chains (α) is decoupled from the β relaxation of the side chains and that both of these relaxation mechanisms are involved in distinct long-range charge-migration processes that exhibit VTF behavior. The comparison of Figure 14c and Figure 14d indicates that the proton delocalization and mobility in the PFIA dry membrane is higher than those in the dry PFSA material. Compared to the dry materials, in the wet membranes the σ_i conductivities increase by at least 4 orders of magnitude in agreement with Figure 11, thereby indicating that water clusters embedded in the bulk membranes dissociate the acid groups as discussed above. For the wet PFSA, a sharper dispersion in the distribution of the hydrophobic domains is observed, which probably reduces the number of IP conductivity pathways. In regions I, II, and III, the IPs show conductivity values that are smaller than those of σ_{EP} (see Figure 14b). This is clearly proven by the behavior of $\phi_{EP} \approx 1$ *vs.* 1/T shown in Figure S18, which demonstrate that at $T \leq 0°C$ the overall conductivity of PFSA is dominated by the σ_{EP} conductivity ($\sigma_T \approx \sigma_{EP}$). At $T = T_m \approx 0°C$ (see Figure 14b and Figure 14d), a steep increase of the conductivity of two orders of magnitude is observed, that confirms that the clusters of the water domains in PFSA are larger than those in the PFIA. In region IV ($0 \leq T \leq T_\alpha \approx 50°C$), the overall conductivity is the superposition of both σ_{EP} and $\sigma_{IP,3}$ (Figure 14b and S18d), thereby indicating that these latter two conductivity pathways both contribute to the overall conductivity in this region.

The wet PFIA shows a behavior that is opposite to that of the PFSA. Indeed, a careful analysis of Figure 14a and Figure 14c clearly reveals that in the wet PFIA in regions I, II and III, the overall conductivity is dominated by $\sigma_{IP,1}$ ($\sigma_T \approx \sigma_{IP,1}$), whereas at higher temperatures (IV and V), the conductivity is associated with the σ_{EP} ($\sigma_T \approx \sigma_{EP}$). This effect is more evident at $T < 0°C$ (I, II and III regions), where the inhibition of the dynamics of the water molecules in hydrophilic domains amplifies the effect of the

side chain interactions, membrane structural features, and polymer matrix relaxations on the conduction pathways. Indeed, it is observed that at T < 0 °C, PFIA conductivity is due to a better delocalized proton and more flexible side chains with smaller water clusters than in PFSA, where the water clusters are larger and the side chain dynamics is significantly inhibited. Finally, the examination of the dependence of the relaxation frequencies on reciprocal temperature (see Figure S20 and discussion) demonstrates that in the PFIA the segmental motion of the perfluorinated backbone chains and the local fluctuation dynamics of side chains are facilitated and more mobile than those in PFSA, which is again attributed to the different distributions of the helical conformations in the hydrophobic domains. To clarify how the dielectric relaxations, which characterize the host ionomer, are involved in each of the different conductivity pathways, the σ_i *vs.* 1/T curves in all the regions of Figure 14(a-b) and f_i *vs.* 1/T profiles in Figure S20 that show VTF behavior are fit to determine the activation energies. The correlation plot shown in Figure 15 allows the comparison of the pseudo-activation energy values of the conduction pathways (determined on σ_i *vs.* 1/T profiles) with $E_{a,i}$ values of the dielectric relaxations (determined on f_i *vs.* 1/T profiles) for both the dry (Figure 15a and 15c) and wet (Figure 15b and 15d) membranes, respectively. Figure 15a shows that, in dry conditions, the activation energy of the β relaxation coincides with that of σ_{EP} in both the I and II regions. In I, $E_a(\sigma_{EP}) \approx 10$ kJ/mole = $E_a(\beta)$ while in II $E_a(\sigma_{EP}) \approx E_a(\beta) \approx 30$ kJ/mole. This indicates that in the dry PFSA, in all temperature ranges examined, the overall conductivity corresponding to σ_{EP} is modulated by the local fluctuation of the R-SO_3H side groups. This latter relaxation, as previously shown,[5a] is strongly coupled with the segmental motions of the perfluorinated backbone chains.

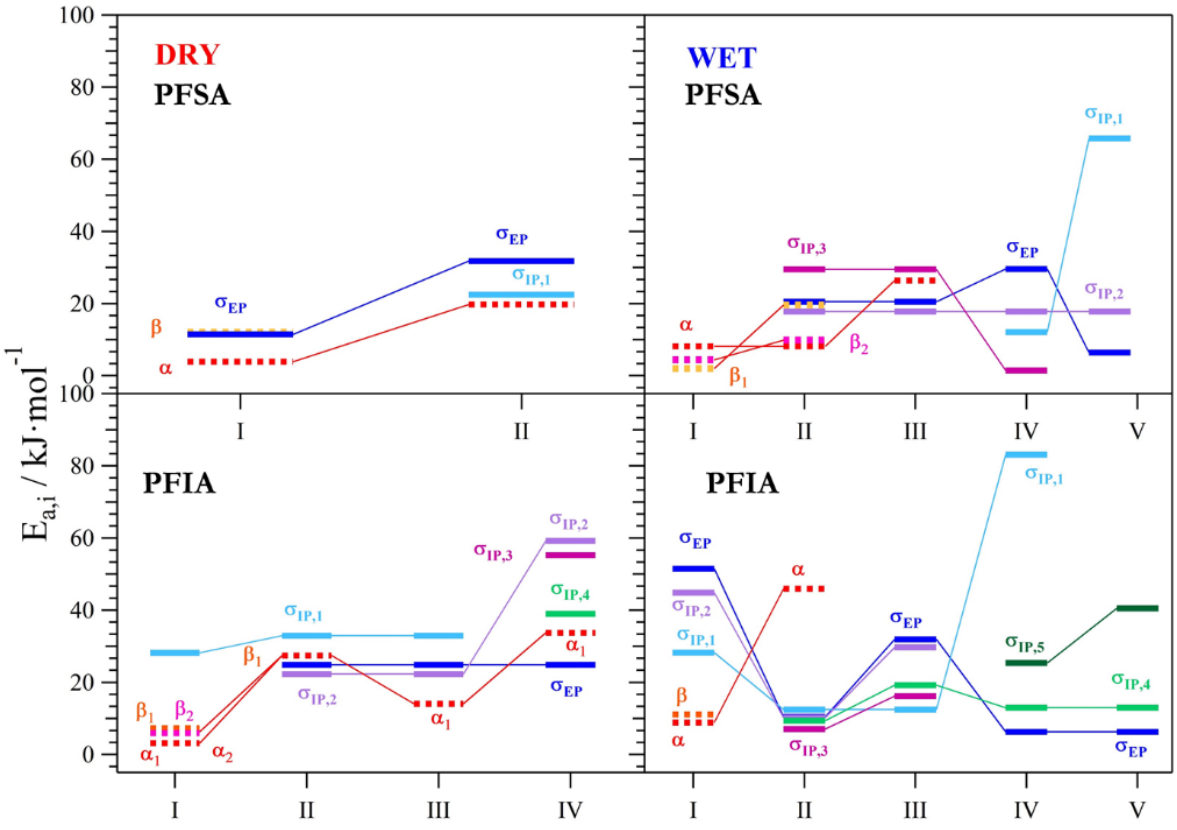

Figure 15. Activation Energies ($E_{a,i}$) of σ_i ($\sigma_i = \sigma_{EP}$, $\sigma_{IP,j}$ with j=1-6) and $f_{r,i}$ dielectric modes in the temperature regions (from I to VI) for PFIA (c, d) and PFSA (a, b) in dry (a, c) and wet (b, d) conditions. The compared values are determined by fitting the data of Figure S20 with an Arrhenius or VTF equation.

For the dry PFIA, a different scenario is revealed. Indeed, in regions I and II, the E_a of the β_1 and β_2 relaxations (Figure 15c) are of the same order of magnitude as $\sigma_{IP,1}$, which, in these regions, is governing the overall conductivity of the membrane ($\sigma_T \approx \sigma_{IP,1}$). However, at T > 40 °C (regions III and IV), the $E_a(\sigma_{EP})$ is of the same order of magnitude as $E_a(\alpha)$. This demonstrates that in regions III and IV the overall conductivity $\sigma_T \approx \sigma_{EP} + \sigma_{IP,1}$ is modulated mainly by the segmental motion of the perfluorinated backbone chains. In the wet membranes (Figure 15b and d), it is observed that for PFSA in all the

investigated temperature regions $E_a(\sigma_{EP}) \approx E_a(\beta_1) \approx E_a(\beta_2) \approx E_a(\alpha)$. Instead, for PFIA, at T < 0 °C (I, II and III regions), $E_a(\sigma_{IP,1}) \approx E_a(\beta_2)$ and T ≥ 0 °C (IV and V regions) $E_a(\sigma_{EP}) \approx E_a(\beta_2)$. These results allow us to summarize that in dry conditions the overall conductivity of the PFSA and PFIA at T < 40 °C are different. In the PFSA σ_T coincides with σ_{EP}, while in PFIA σ_T corresponds to $\sigma_{IP,1}$. In the PFSA, σ_{EP} is modulated by the β and α relaxations, while $\sigma_{IP,1}$ of the PFIA by the β_1 and β_2 modes. At T > 40 °C, $\sigma_T \approx \sigma_{EP}$ for both PFSA and PFIA. σ_{EP} in the PFSA is correlated to the dielectric relaxations in the order β >> α, while in PFIA it is directly related to the α relaxation. In wet conditions, for PFSA, $\sigma_T \approx \sigma_{EP}$ in all of the explored temperature regions and σ_{EP} is significantly modulated by both the α and β_1 and β_2 relaxations. For PFIA, at T < 0 °C, $\sigma_T \approx \sigma_{IP,1}$ and $\sigma_{IP,1}$ is modulated by the β_2, the relaxation event of the side chains characterized by the inter-side chain interactions. At T ≥ 0 °C, $\sigma_T \approx \sigma_{EP}$, *i.e.*, in σ_{EP} pathway β_2 relaxation plays a crucial role in long range charge migration events. Finally, further insights can be obtained by correlating the diffusion coefficient[55] associated to each σ_i to the frequency of each relaxation mode (α, α_1, α_2, β, β_1 and β_2) for both the dry and wet PFSA and PFIA membranes (See Figure S21). From this analysis, it is confirmed that the dielectric relaxations discussed above play a crucial role in modulating the conductivity pathways revealed in each temperature region and for both the dry and wet PFSA and PFIA membranes. Using these values, one can also calculate the average migration distance, $\langle r_i \rangle$, for the various polarization phenomena[22, 43b, 55] as shown in Figure 16. The figure shows that as the temperature increases, $\langle r_i \rangle$ values of conduction pathways of both dry and wet PFSA and PFIA rises. This evidence proves that the charge-migration processes in all of the revealed conduction pathways of materials are thermally stimulated phenomena.

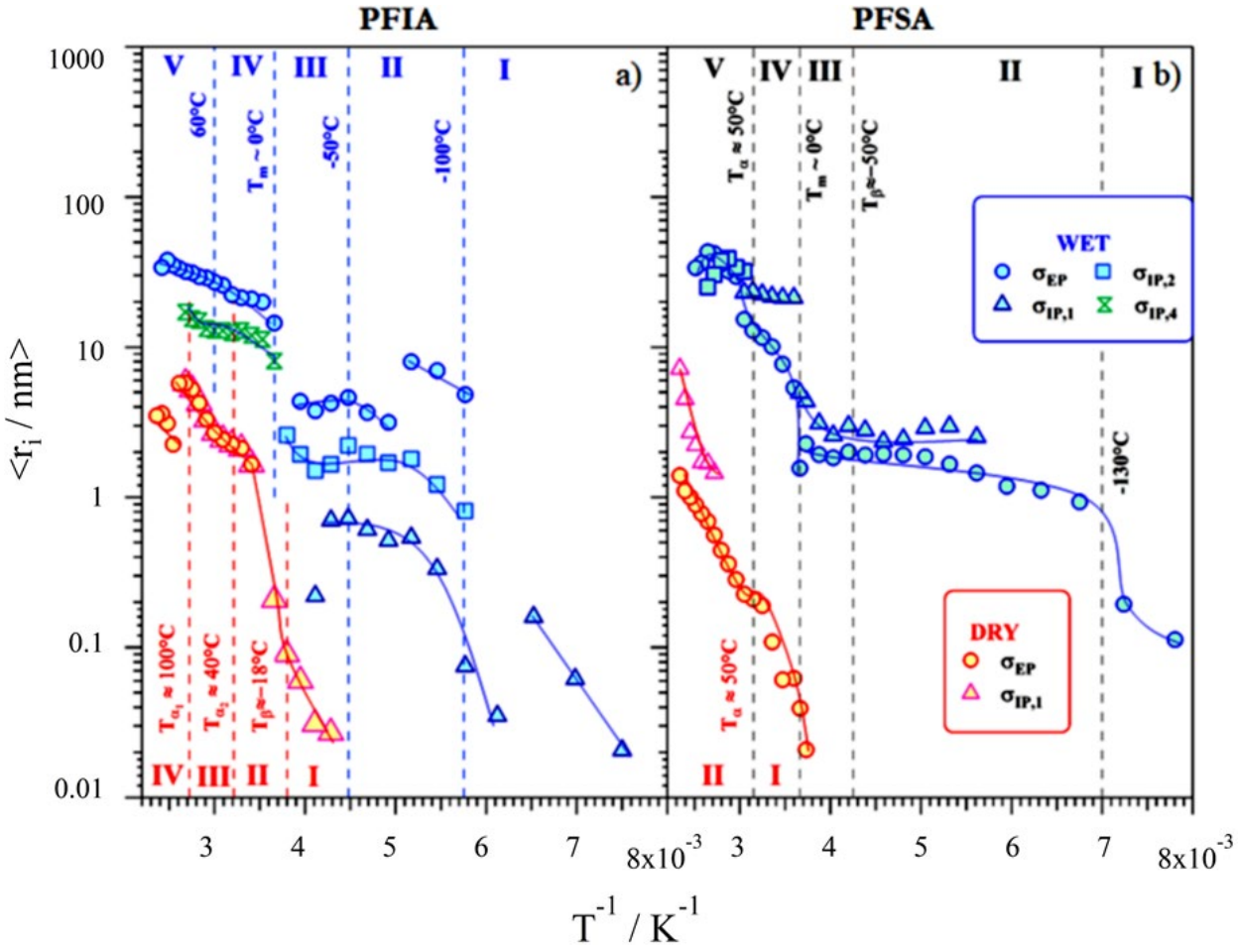

Figure 16. Dependence of the average migration distance, $< r_i >$, (for σ_{EP} and $\sigma_{IP,i}$ with i = 1 to 6) *vs.* inverse of temperature for PFIA (a) and PFSA (b) in dry and wet membranes.

In accordance with results reported elsewhere,[5a, 22, 55] σ_{EP} conductivity pathways occur owing to the exchange of protons between delocalization bodies (DBs). The DB concept was recently proposed for other perfluorinated membranes.[4,15a] A DB is a volume of the material, which includes both a hydrophilic and a hydrophobic component. In a DB, the migrating proton with respect to the timescale of conductivity is exchanged so fast between coordination sites so as to be considered delocalized. The $\sigma_{IP,1}$ conductivity pathways takes place at the interfaces between domains with different permittivity as follows: i) in the wet membrane, there is a percolation pathway where the proton is exchanged between $[H^+(H_2O)_n]$

clusters neutralizing the anionic charge of the side chains; and ii) in the dry membrane, there is a percolation pathway formed by simple proton-exchange processes between interacting sites located in neighboring polar side chains.[22] Our results allude to the role of multi-acid side chain in effectively reducing EW and underscores the role of polymer dynamics in ion transport, in addition to the water dynamics, especially at low hydration levels.

CONCLUSIONS

A double-acid functionalized PFIA polymer was fully investigated and compared with its single-acid functionalized PFSA analogue. The initial design of this polymer was to utilize the mechanical strength of the more crystalline PTFE backbone of the single-acid functionalized PFSA by simply adding a second dissociable protogenic group to the side chain to increase charge carriers without compromising mechanical integrity. However, the real situation is much more complex. The PFIA exhibits both intra- and inter-side chain interactions that manifest themselves in the onset of the thermal decomposition of the polymer being lower than of the PFSA analogue. This is confirmed in the IR where the ν(S-OH) and other bands are split into two bands. From the MD studies it is shown that 60% of the side chains are curved forming intra-chain rings, while the remaining 40% maintain their linear extended structure interacting with the neighboring side chains. Both the WAXS and IR indicate that the side chains modulate the polymer backbone to become more organized, crystalline, with distinct interactions between chains confirmed. The SAXS shows a transition at 60 °C and an almost invariant hydrophilic domain size in the PFIA. The proton conductivity of the PFIA is higher than that of the PFSA analogue only at intermediate RHs, at all temperatures studied. From NMR PFGSE measurements and the MD calculations it appears that the charge migration mechanism mediated by proton exchange processes between coordination sites at the hydrophobic-hydrophilic interfaces predominates in the PFIA material.

While the structure and conductivity of PFIA and PFSA becomes comparable in fully-hydrated state, their nanostructure and proton dissociation and transfer differ at low hydration levels, where PFIA exhibits better performance, owing to its less disordered structure and increased segmental dynamics of polymer chains facilitated by the presence of imide-group. The change in the character of the side chain from the PFSA to the PFIA increases the fraction of 10_3 and 2_1 crystalline domains and decreases the abundance of the 15_7 amorphous domain in the polymer backbone. The PFIA absorbs more water molecules (λ) than the PFSA at low RH conditions, which is retained over the entire RH regime. The PFIA is likely to have an additional water molecule even in the dry state, which could be attributed to the primary solvation of the second protogenic group. At high RH, the proton conductivities of the PFSA and PFIA are surprisingly similar. The PFIA clearly has much higher proton conductivity than the PFSA at lower RH and higher temperatures. This indicates that the nanostructure and transport enabled by the longer side chains in the material is more important to the overall proton conductivity than the addition of a second proton and the increase in the IEC. If both protons were fully available for transport and the mechanism remained unchanged, then the PFIA would be expected to have almost 1.5 times the conductivity at 100% RH, but it clearly does not. In dry conditions, the PFSA exhibits one α and one β relaxation, while the PFIA exhibits two α-relaxations (α_1 and α_2) and two β events (β_1 and β_2). The results indicate that in the PFIA the segmental motion of the perfluorinated backbone chains and the local fluctuation dynamics of the side chains are facilitated by this. In addition, it is to be remarked that in the dry state, the PFIA side chains, which are involved in intra-side chain interactions, exhibit a larger relaxation rate. Thus, the local fluctuations of these side chains are significantly facilitated. This is perfectly in agreement with the results of the thermal, X-Ray, and vibrational studies. In detail:

a) in dry PFSA, the conductivity occurs in all the investigated temperature ranges by exchange of the proton between DBs in all the temperature ranges investigated. In this case, the delocalization of the proton between DBs requires the coupling between the α and β relaxations of the host

matrix. Also, $<r_{EP}>$ region I (T < -50 °C) are below 2 Å, thereby indicating that the proton is exchanged between interacting neighboring R-SO_3H acid sites. For region II (T ≥ -50°C), $<r_{EP}>$ increases up to 20 Å, thus indicating that thermal stimulation facilitates the delocalization of the protons forming very small DBs with sizes increasing with T. These results are in accordance with the WAXS results and suggest that these DBs are present at the interfaces of lamellar crystalline domains with the perfluorinated backbone chains in a 2_1 helical conformation as discussed above. In this case, the distance between the interacting acid side chains is of the order of 2 nm and the delocalization of the proton in the DBs results in possible migration distances of the order of 20 Å.

b) in dry PFIA, at T < 40 °C, the conductivity occurs by a hopping processes between the polar side chains and these processes are modulated by the β and α relaxations. Also, $<r_{IP,1}>$ increases on T from *ca*. 2 Å up to ca. 40 Å and in region III, $<r_{EP}>$ ranges from *ca.* 20 to *ca.* 40 Å and is overlapped with $<r_{IP,1}>$. These results are in accordance with the nanostructural data, thereby confirming that crystalline domains with 10_3 and 2_1 helical conformations are crucial for promoting the long-range charge-migration events in dry conditions. For T ≥ 40 °C, $<r_{EP}>$ presents an average value of *ca*. 36 Å which confirms, in accordance with other studies,[55] that the *d*-spacing of the ionomer peak in SAXS coincides with the average $<r_{EP}>$ at high temperature. Furthermore, at T > 40°C, the long-range charge migration in PFIA occurs owing to the H^+ exchange phenomena between DBs and these events are triggered by the α-relaxation modes of the perfluorinated backbone chains.

c) In the wet PFSA, in all of the explored temperature range, the migration of H^+ occurs by exchanges between DBs and these phenomenon are modulated by the dielectric relaxation events of host matrix in the order $\alpha > \beta_1 > \beta_2$. The regions present an average value of *ca*. 20 Å, while at T > 0 °C (IV and V regions) it exhibits a value approximately of 30 Å. Also in this case, the

hydrated structural data are in accordance with the average migration distances indicating that the expected size of the DBs are of the same order of magnitude of the structural periodicities determined by scattering analysis (see Figure 7).

d) For the wet PFIA, at T < 0 °C the conductivity occurs by exchange events of the proton between clusters of acid water $[H^+(H_2O)_n]$, neutralizing the negative charge delocalized in the flexible side chains of the polymer located at the interfaces between the domains with different permittivity. This phenomenon occurs efficiently when hydrophobic domains of PFIA consists of perfluorinated backbone chains with 2_1 conformational geometries are close-packed to form lamellas with small sizes, where $\langle r_{EP} \rangle$ is *ca.* 7 Å. As expected, this migration process is modulated by the β_2 relaxation. For T ≥ 0 °C, $\langle r_{EP} \rangle$ rises from *ca.* 10 to *ca.* 38 Å (in agreement with Figure 6) and the long-range proton-migration events occur owing to charge-exchange phenomena between DBs whose size is reflecting the *d*-spacing. In this case, the DBs include small clusters of acid water solvating the side chains involved in intra- and inter-side chain interactions. These migration phenomena are significantly promoted by the β_2 relaxation, *i.e.*, by the local fluctuation of dipole moment of side chains with intra-side chain interactions.

ASSOCIATED CONTENT

In the Supporting information file more details on FT-IR ATR, SAXS, NMR and Broadband Electrical Spectroscopy measurements, as well as Molecular simulations are reported.

AUTHOR INFORMATION

Corresponding Author

*prof. Vito Di Noto, University of Padova, Section of Chemistry for Technology, Department of Industrial Engineering, Via F. Marzolo 9, 35131 Padova, Italy

e-mail: vito.dinoto@unipd.it

*prof. Andrew M. Herring, Department of Chemical and Biological Engineering, Colorado School of Mines, Golden, CO 80401, USA

e-mail: aherring@mines.edu

Author Contributions

The manuscript was written through contributions of all authors. All authors have given approval to the final version of the manuscript and they had contributed equally.

Funding Sources and ACKNOWLEDGMENT

Work by AK and AZW was funded under the Fuel Cell Performance and Durability Consortium (FC-PAD), by the Fuel Cell Technologies Office (FCTO), of the office of the Energy Efficiency and Renewable Energy (EERE), of the U. S. Department of Energy under contract number DE-AC02-05CH11231 and Program Development Manager Dimitrios Papageorgopoulos.

This material is in part based upon work performed by the Joint Center for Artificial Photosynthesis (JCAP), a DOE Energy Innovation Hub, supported through the Office of Science of the U.S. Department of Energy under award number DE-SC0004993 during AMHs sabbatical.

This work made use of facilities at the Advanced Light Source (ALS), supported by the Office of Science, Office of Basic Energy Sciences, of the U.S. Department of Energy (Contract No. DE-AC02-05CH11231).

This research used resources of the Advanced Photon Source, a U.S. Department of Energy (DOE) Office of Science User Facility operated for the DOE Office of Science by Argonne National Laboratory under Contract No. DE-AC02-06CH11357.

KV, GN and VDN thanks the University of Padova for the finantial support under the project "Advanced electrolytes for next-generation Anion-Exchange Membrane Fuel Cells - AGNI" (project number BIRD164837/16).

VDN wishes to thank the Universidad Carlos III de Madrid for assigning him the "Catedras de Excelencia".

REFERENCES

1. (a) Chu, S.; Majumdar, A., Opportunities and challenges for a sustainable energy future. *Nature* **2012,** *488* (7411), 294-303; (b) Obama, B., The irreversible momentum of clean energy. *Science* **2017,** *355* (6321), 126-129.

2. Yoshida, T.; Kojima, K., Toyota MIRAI Fuel Cell Vehicle and Progress Toward a Future Hydrogen Society. *The Electrochemical Society Interface* **2015,** *24* (2), 45-49.

3. (a) Kusoglu, A.; Weber, A. Z., New Insights into Perfluorinated Sulfonic-Acid Ionomers. *Chemical Reviews* **2017,** *117* (3), 987-1104; (b) Papageorgopoulos, D., Fuel Cells Overview. In *DoE 2015 Annual Merit Review Meeting*, available at http://www.hydrogen.energy.gov: 2015.

4. (a) Kreuer, K.-D.; Paddison, S. J.; Spohr, E.; Schuster, M., Transport in Proton Conductors for Fuel-Cell Applications: Simulations, Elementary Reactions, and Phenomenology. *Chemical Reviews* **2004,** *104* (10), 4637-4678; (b) Kreuer, K.-D.; Dippel, T.; Meyer, W.; Maier, J., Nafion® Membranes:

Molecular Diffusion, Proton Conductivity and Proton Conduction Mechanism. *MRS Proceedings* **2011,** *293*, 273 (10 pages); (c) Crothers, A. R.; Radke, C. J.; Weber, A. Z., Impact of Nano- and Mesoscales on Macroscopic Cation Conductivity in Perfluorinated-Sulfonic-Acid Membranes. *Journal of Physical Chemistry C* **2017,** *121* (51), 28262-28274; (d) Maalouf, M.; Sun, C. N.; Pyle, B.; Emery, M.; Haugen, G. M.; Hamrock, S. J.; Zawodzinski, T. A., Factors enabling high mobility of protons and water in perfluorosulfonate membranes under low hydration conditions. *International Journal of Hydrogen Energy* **2014,** *39* (6), 2795-2800; (e) Berrod, Q.; Lyonnard, S.; Guillermo, A.; Ollivier, J.; Frick, B.; Manseri, A.; Ameduri, B.; Gebel, G., Nanostructure and Transport Properties of Proton Conducting Self-Assembled Perfluorinated Surfactants: A Bottom-Up Approach toward PFSA Fuel Cell Membranes. *Macromolecules* **2015,** *48* (17), 6166-6176.

5. (a) Giffin, G. A.; Haugen, G. M.; Hamrock, S. J.; Di Noto, V., Interplay between structure and relaxations in perfluorosulfonic acid proton conducting membranes. *Journal of the American Chemical Society* **2013,** *135* (2), 822-34; (b) Kreuer, K. D.; Schuster, M.; Obliers, B.; Diat, O.; Traub, U.; Fuchs, A.; Klock, U.; Paddison, S. J.; Maier, J., Short-side-chain proton conducting perfluorosulfonic acid ionomers: Why they perform better in PEM fuel cells. *Journal of Power Sources* **2008,** *178* (2), 499-509.

6. (a) Di Noto, V.; Gliubizzi, R.; Negro, E.; Pace, G., Effect of SiO_2 on relaxation phenomena and mechanism of ion conductivity of [Nafion/$(SiO_2)_x$] composite membranes. *Journal of Physical Chemistry B* **2006,** *110* (49), 24972-24986; (b) Di Noto, V.; Lavina, S.; Negro, E.; Vittadello, M.; Conti, F.; Piga, M.; Pace, G., Hybrid inorganic-organic proton conducting membranes based on Nafion and 5 wt% of M_xO_y (M = Ti, Zr, Hf, Ta and W). Part II: Relaxation phenomena and conductivity mechanism. *Journal of Power Sources* **2009,** *187* (1), 57-66.

7. (a) Madsen, L. A.; Hou, J., Chapter 14. NMR Diffusometry for the Study of Energy-related Soft Materials. In *Diffusion NMR of Confined Systems*, The Royal Society of Chemistry: 2016; pp 464-496; (b) Perrin, J. C.; Lyonnard, S.; Guillermo, A.; Levitz, P., Water dynamics in ionomer membranes by

field-cycling NMR relaxometry. *Magn Reson Imaging* **2007,** *25* (4), 501-4; (c) Lee, D. K.; Saito, T.; Benesi, A. J.; Hickner, M. A.; Allcock, H. R., Characterization of Water in Proton-Conducting Membranes by Deuterium NMR T-1 Relaxation. *Journal of Physical Chemistry B* **2011,** *115* (5), 776-783.

8. (a) Tse, Y. L. S.; Herring, A. M.; Kim, K.; Voth, G. A., Molecular Dynamics Simulations of Proton Transport in 3M and Nafion Perfluorosulfonic Acid Membranes. *Journal of Physical Chemistry C* **2013,** *117* (16), 8079-8091; (b) Cui, S.; Liu, J.; Selvan, M. E.; Paddison, S. J.; Keffer, D. J.; Edwards, B. J., Comparison of the hydration and diffusion of protons in perfluorosulfonic acid membranes with molecular dynamics simulations. . *Journal of Physical Chemistry B* **2008,** *112* (42), 13273-84; (c) Paddison, S. J.; Elliott, J. A., The effects of backbone conformation on hydration and proton transfer in the 'short-side-chain' perfluorosulfonic acid membrane. *Solid State Ionics* **2006,** *177* (26-32), 2385-2390; (d) Paddison, S. J.; Elliott, J. A., On the consequences of side chain flexibility and backbone conformation on hydration and proton dissociation in perfluorosulfonic acid membranes. *Physical Chemistry Chemical Physics* **2006,** *8* (18), 2193-203; (e) Elliott, J. A.; Paddison, S. J., Modelling of morphology and proton transport in PFSA membranes. *Physical Chemistry Chemical Physics* **2007,** *9* (21), 2602-2618; (f) Wu, D. S.; Paddison, S. J.; Elliott, J. A., Effect of Molecular Weight on Hydrated Morphologies of the Short-Side-Chain Perfluorosulfonic Acid Membrane. *Macromolecules* **2009,** *42* (9), 3358-3367; (g) Wu, D. S.; Paddison, S. J.; Elliott, J. A., A comparative study of the hydrated morphologies of perfluorosulfonic acid fuel cell membranes with mesoscopic simulations. *Energy & Environmental Science* **2008,** *1* (2), 284-293; (h) Dorenbos, G.; Suga, Y., Simulation of equivalent weight dependence of Nafion morphologies and predicted trends regarding water diffusion. *Journal of Membrane Science* **2009,** *330* (1-2), 5-20; (i) Clark, J. K.; Paddison, S. J., Proton dissociation and transfer in proton exchange membrane ionomers with multiple and distinct pendant acid groups: An ab initio study. *Electrochimica Acta* **2013,** *101* (0), 279-292; (j) Clark, J. K., 2nd; Paddison, S. J.; Hamrock, S. J.,

The effect of hydrogen bond reorganization and equivalent weight on proton transfer in 3M perfluorosulfonic acid ionomers. *Physical Chemistry Chemical Physics* **2012,** *14* (47), 16349-59; (k) Clark, J. K.; Paddison, S. J., The effect of side chain connectivity and local hydration on proton transfer in 3M perfluorosulfonic acid membranes. *Solid State Ionics* **2012,** *213*, 83-91.

9. (a) Feng, S. L.; Savage, J.; Voth, G. A., Effects of Polymer Morphology on Proton Solvation and Transport in Proton-Exchange Membranes. *Journal of Physical Chemistry C* **2012,** *116* (36), 19104-19116; (b) Savage, J.; Voth, G. A., Proton Solvation and Transport in Realistic Proton Exchange Membrane Morphologies. *Journal of Physical Chemistry C* **2016,** *120* (6), 3176-3186.

10. (a) Danilczuk, M.; Lin, L.; Schlick, S.; Hamrock, S. J.; Schaberg, M. S., Understanding the fingerprint region in the infra-red spectra of perfluorinated ionomer membranes and corresponding model compounds: Experiments and theoretical calculations. *Journal of Power Sources* **2011,** *196* (20), 8216-8224; (b) Devanathan, R.; Dupuis, M., Insight from molecular modelling: does the polymer side chain length matter for transport properties of perfluorosulfonic acid membranes? *Physical Chemistry Chemical Physics* **2012,** *14* (32), 11281-11295.

11. (a) Kusoglu, A.; Dursch, T. J.; Weber, A. Z., Nanostructure/Swelling Relationships of Bulk and Thin-Film PFSA Ionomers. *Advanced Functional Materials* **2016,** *26* (27), 4961-4975; (b) Economou, N. J.; O'Dea, J. R.; McConnaughy, T. B.; Buratto, S. K., Morphological differences in short side chain and long side chain perfluorosulfonic acid proton exchange membranes at low and high water contents. *RSC Advances* **2013,** *3* (42), 19525-19532; (c) Hamrock, S. J.; Herring, A. M., Proton Exchange Membrane Fuel Cells: High-Temperature, Low-Humidity Operation. In *Encyclopedia of Sustainability Science and Technology*, Meyers, R., Ed. Springer New York: 2012; pp 8328-8347.

12. (a) Devanathan, R.; Venkatnathan, A.; Dupuis, M., Atomistic simulation of nafion membrane. 2. Dynamics of water molecules and hydronium ions. *Journal of Physical Chemistry B* **2007,** *111* (45), 13006-13; (b) Devanathan, R.; Venkatnathan, A.; Dupuis, M., Atomistic simulation of nafion membrane:

I. Effect of hydration on membrane nanostructure. *Journal of Physical Chemistry B* **2007,** *111* (28), 8069-79.

13. Agmon, N., The Grotthuss Mechanism. *Chemical Physics Letters* **1995,** *244* (5-6), 456-462.

14. (a) Page, K. A.; Rowe, B. W.; Masser, K. A.; Faraone, A., The effect of water content on chain dynamics in nafion membranes measured by neutron spin echo and dielectric spectroscopy. *Journal of Polymer Science Part B: Polymer Physics* **2014**, n/a-n/a; (b) Moilanen, D. E.; Piletic, I. R.; Fayer, M. D., Water Dynamics in Nafion Fuel Cell Membranes: the Effects of Confinement and Structural Changes on the Hydrogen Bond Network. *J Phys Chem C Nanomater Interfaces* **2007,** *111* (25), 8884-8891; (c) Daly, K. B.; Benziger, J. B.; Debenedetti, P. G.; Panagiotopoulos, A. Z., Molecular dynamics simulations of water sorption in a perfluorosulfonic acid membrane. *J Phys Chem B* **2013,** *117* (41), 12649-60; (d) Hickner, M. A., Water-mediated transport in ion-containing polymers. *Journal of Polymer Science Part B-Polymer Physics* **2012,** *50* (1), 9-20.

15. (a) Kreuer, K. D.; Rabenau, A.; Weppner, W., Vehicle Mechanism, a New Model for the Interpretation of the Conductivity of Fast Proton Conductors. *Angewandte Chemie-International Edition in English* **1982,** *21* (3), 208-209; (b) Kreuer, K. D., On the development of proton conducting materials for technological applications. *Solid State Ionics* **1997,** *97* (1-4), 1-15; (c) Kreuer, K. D., On the development of proton conducting polymer membranes for hydrogen and methanol fuel cells. *Journal of Membrane Science* **2001,** *185* (1), 29-39.

16. Tuckerman, M.; Laasonen, K.; Sprik, M.; Parrinello, M., Ab-Initio Molecular-Dynamics Simulation of the Solvation and Transport of H_3O^+ and OH^- Ions in Water. *Journal of Physical Chemistry* **1995,** *99* (16), 5749-5752.

17. (a) Paddison, S. J.; Paul, R.; Zawodzinski, T. A., A statistical mechanical model of proton and water transport in a proton exchange membrane. *Journal of the Electrochemical Society* **2000,** *147* (2), 617-626; (b) Paddison, S. J.; Paul, R.; Zawodzinski, T. A., Proton friction and diffusion coefficients in

hydrated polymer electrolyte membranes: Computations with a non-equilibrium statistical mechanical model. *Journal of Chemical Physics* **2001,** *115* (16), 7753-7761; (c) Paddison, S. J.; Paul, R., The nature of proton transport in fully hydrated Nafion(R). *Physical Chemistry Chemical Physics* **2002,** *4* (7), 1158-1163; (d) Paddison, S. J., Proton conduction mechanisms at low degrees of hydration in sulfonic acid-based polymer electrolyte membranes. *Annual Review of Materials Research* **2003,** *33*, 289-319; (e) Paddison, S. J.; Zawodzinski, T. A., Molecular modeling of the pendant chain in Nafion (R). *Solid State Ionics* **1998,** *113*, 333-340.

18. (a) Habenicht, B. F.; Paddison, S. J.; Tuckerman, M. E., Ab initio molecular dynamics simulations investigating proton transfer in perfluorosulfonic acid functionalized carbon nanotubes. *Phys Chem Chem Phys* **2010,** *12* (31), 8728-32; (b) Habenicht, B. F.; Paddison, S. J.; Tuckerman, M. E., The effects of the hydrophobic environment on proton mobility in perfluorosulfonic acid systems: an ab initio molecular dynamics study. *Journal of Materials Chemistry* **2010,** *20* (30), 6342-6351.

19. Di Noto, V.; Piga, M.; Lavina, S.; Negro, E.; Yoshida, K.; Ito, R.; Furukawa, T., Structure, properties and proton conductivity of Nafion/$[(TiO_2)\cdot(WO_3)_{0.148}]_{\psi}TiO_2$ nanocomposite membranes. *Electrochimica Acta* **2010,** *55* (4), 1431-1444.

20. Di Noto, V.; Piga, M.; Pace, G.; Negro, E.; Lavina, S., Dielectric Relaxations and Conductivity Mechanism of Nafion: Studies Based on Broadband Dielectric Spectroscopy. *ECS Transactions* **2008,** *16* (2), 1183-1193.

21. Hofmann, D. W. M.; Kuleshova, L.; D'Aguanno, B.; Di Noto, V.; Negro, E.; Conti, F.; Vittadello, M., Investigation of Water Structure in Nafion Membranes by Infrared Spectroscopy and Molecular Dynamics Simulation. *The Journal of Physical Chemistry B* **2009,** *113* (3), 632-639.

22. Di Noto, V.; Piga, M.; Giffin, G. A.; Vezzu, K.; Zawodzinski, T. A., Interplay between Mechanical, Electrical, and Thermal Relaxations in Nanocomposite Proton Conducting Membranes

Based on Nafion and a [$(ZrO_2)\cdot(Ta_2O_5)_{0.119}$] Core-Shell Nanofiller. *Journal of the American Chemical Society* **2012,** *134* (46), 19099-19107.

23. Di Noto, V.; Piga, M.; Giffin, G. A.; Lavina, S.; Smotkin, E. S.; Sanchez, J.-Y.; Iojoiu, C., Influence of Anions on Proton-Conducting Membranes Based on Neutralized Nafion 117, Triethylammonium Methanesulfonate, and Triethylammonium Perfluorobutanesulfonate. 1. Synthesis and Properties. *The Journal of Physical Chemistry C* **2012,** *116* (1), 1361-1369.

24. Schaberg, M. S.; Abulu, J. E.; Haugen, G. M.; Emery, M. A.; O'Conner, S. J.; Xiong, P. N.; Hamrock, S., New Multi Acid Side-Chain Ionomers for Proton Exchange Membrane Fuel Cells. *ECS Transactions* **2010,** *33* (1), 627-633.

25. Emery, M.; Frey, M.; Guerra, M.; Haugen, G.; Hintzer, K.; Lochhaas, K. H.; Pham, P.; Pierpont, D.; Schaberg, M.; Thaler, A.; Yandrasits, M.; Hamrock, S., The Development of New Membranes for Proton Exchange Membrane Fuel Cells. *ECS Transactions* **2007,** *11* (1), 3-14.

26. Paddison, S. J.; Elliott, J. A., Molecular modeling of the short-side-chain perfluorosulfonic acid membrane. *Journal of Physical Chemistry A* **2005,** *109* (33), 7583-93.

27. Economou, N. J.; Barnes, A. M.; Wheat, A. J.; Schaberg, M. S.; Hamrock, S. J.; Buratto, S. K., Investigation of Humidity Dependent Surface Morphology and Proton Conduction in Multi-Acid Side Chain Membranes by Conductive Probe Atomic Force Microscopy. *Journal of Physical Chemistry B* **2015,** *119* (44), 14280-14287.

28. Di Noto, V.; Boaretto, N.; Negro, E.; Giffin, G. A.; Lavina, S.; Polizzi, S., Inorganic–organic membranes based on Nafion, [$(ZrO_2)\cdot(HfO_2)_{0.25}$] and [$(SiO_2)\cdot(HfO_2)_{0.28}$]. Part I: Synthesis, thermal stability and performance in a single PEMFC. *International Journal of Hydrogen Energy* **2012,** *37* (7), 6199-6214.

29. Liu, Y.; Horan, J. L.; Schlichting, G. J.; Caire, B. R.; Liberatore, M. W.; Hamrock, S. J.; Haugen, G. M.; Yandrasits, M. A.; Seifert, S. n.; Herring, A. M., A small-angle X-ray scattering study of the

development of morphology in films formed from the 3M perfluorinated sulfonic acid ionomer. *Macromolecules* **2012,** *45* (18), 7495-7503.

30. (a) Kusoglu, A.; Weber, A. Z., Role of Chemical-Mechanical Energies in Understanding Structure and Properties of Aged and Degraded Membranes. *ECS Transactions* **2013,** *50* (2), 961-965; (b) Kusoglu, A.; Cho, K. T.; Prato, R. A.; Weber, A. Z., Structural and transport properties of Nafion in hydrobromic-acid solutions. *Solid State Ionics* **2013,** *252*, 68-74.

31. Case, D. A.; Babin, V.; Berryman, J. T.; Betz, R. M.; Cai, Q.; Cerutti, D. S.; Cheatham, T. E.; Darden, T. A.; Duke, R. E.; Gohlke, H.; Goetz, A. W.; Gusarov, S.; Homeyer, N.; Janowski, P.; Kaus, J.; Kolossváry, I.; Kovalenko, A.; Lee, T. S.; LeGrand, S.; Luchko, T.; Luo, R.; Madej, B.; Merz, K. M.; Paesani, F.; Roe, D. R.; Roitberg, A.; Sagui, C.; Salomon-Ferrer, R.; Seabra, G.; Simmerling, C. L.; Smith, W.; Swails, J.; Walker; Wang, J.; Wolf, R. M.; Wu, X.; Kollman, P. A., *AMBER 14*. San Francisco, 2014.

32. Jorgensen, W. L.; Chandrasekhar, J.; Madura, J. D.; Impey, R. W.; Klein, M. L., Comparison of simple potential functions for simulating liquid water. *The Journal of chemical physics* **1983,** *79* (2), 926-935.

33. (a) Liu, Y.; Sambasivarao, S. V.; Horan, J. L.; Yang, Y.; Maupin, C. M.; Herring, A. M., A Combined Theoretical and Experimental Investigation of the Transport Properties of Water in a Perfluorosulfonic Acid Proton Exchange Membrane Doped with the Heteropoly Acids, $H_3PW_{12}O_{40}$ or $H_4SiW_{12}O_{40}$. *The Journal of Physical Chemistry C* **2014,** *118* (2), 854-863; (b) Sambasivarao, S. V.; Liu, Y.; Horan, J. L.; Seifert, S.; Herring, A. M.; Maupin, C. M., Enhancing Proton Transport and Membrane Lifetimes in Perfluorosulfonic Acid Proton Exchange Membranes: A Combined Computational and Experimental Evaluation of the Structure and Morphology Changes Due to $H_3PW_{12}O_{40}$ Doping. *The Journal of Physical Chemistry C* **2014,** *118* (35), 20193-20202; (c) Kinsinger, C. L.; Liu, Y.; Liu, F. L.; Yang, Y.; Seifert, S.; Knauss, D. M.; Herring, A. M.; Maupin, C. M., Random and Block Sulfonated

Polyaramides as Advanced Proton Exchange Membranes. *Journal of Physical Chemistry C* **2015,** *119* (44), 24724-24732.

34. Wang, J. M.; Wolf, R. M.; Caldwell, J. W.; Kollman, P. A.; Case, D. A., Development and testing of a general amber force field. *Journal of Computational Chemistry* **2004,** *25* (9), 1157-1174.

35. Frisch, M. J.; Trucks, G. W.; Schlegel, H. B.; Scuseria, G. E.; Robb, M. A.; Cheeseman, J. R.; Scalmani, G.; Barone, V.; Mennucci, B.; Petersson, G. A., Gaussian 09 C. 01. *Gaussian Inc., Wallingford CT* **2009**.

36. Bayly, C. I.; Cieplak, P.; Cornell, W. D.; Kollman, P. A., A well-behaved electrostatic potential based method using charge restraints for deriving atomic charges: the RESP model. *Journal of Physical Chemistry* **1993,** *97* (40), 10269-10280.

37. Wang, J.; Wang, W.; Kollman, P. A.; Case, D. A., Automatic atom type and bond type perception in molecular mechanical calculations. *Journal of molecular graphics and modelling* **2006,** *25* (2), 247-260.

38. (a) Sambasivarao, S. V.; Acevedo, O., Development of OPLS-AA Force Field Parameters for 68 Unique Ionic Liquids. *Journal of Chemical Theory and Computation* **2009,** *5* (4), 1038-1050; (b) Bharadwaj, V. S.; Eagan, N. M.; Wang, N. M.; Liberatore, M. W.; Maupin, C. M., Molecular Simulations of Fatty-Acid Methyl Esters and Representative Biodiesel Mixtures. *Chemphyschem* **2015,** *16* (13), 2810-2817; (c) Slingsby, J. G.; Vyas, S.; Maupin, C. M., A charge-modified general amber force field for phospholipids: improved structural properties in the tensionless ensemble. *Molecular Simulation* **2015,** *41* (18), 1449-1458; (d) Bharadwaj, V. S.; Dean, A. M.; Maupin, C. M., Insights into the glycyl radical enzyme active site of benzylsuccinate synthase: a computational study. *Journal of the American Chemical Society* **2013,** *135* (33), 12279-12288; (e) Schutt, T. C.; Hegde, G. A.; Bharadwaj, V. S.; Johns, A. J.; Maupin, C. M., Impact of Water-Dilution on the Biomass Solvation Properties of the Ionic Liquid

1-Methyltriethoxy-3-Ethylimidazolium Acetate. *The Journal of Physical Chemistry B* **2017,** *121* (4), 843-853.

39. Knox, C. K.; Voth, G. A., Probing selected morphological models of hydrated Nafion using large-scale molecular dynamics simulations. *The Journal of Physical Chemistry B* **2010,** *114* (9), 3205-3218.

40. Martinez, L.; Andrade, R.; Birgin, E. G.; Martinez, J. M., PACKMOL: A Package for Building Initial Configurations for Molecular Dynamics Simulations. *Journal of Computational Chemistry* **2009,** *30* (13), 2157-2164.

41. Di Noto, V.; Piga, M.; Negro, E.; Giffin, G. A.; Polizzi, S.; Zawodzinski, T. A., New nanocomposite proton conducting membranes based on a core-shell nanofiller for low relative humidity fuel cells. *RSC Advances* **2013,** *3* (41), 18960-18969.

42. (a) Aieta, N. V.; Stanis, R. J.; Horan, J. L.; Yandrasits, M. A.; Cookson, D. J.; Ingham, B.; Toney, M. F.; Hamrock, S. J.; Herring, A. M., Clipped Random Wave Morphologies and the Analysis of the SAXS of an Ionomer Formed by Copolymerization of Tetrafluoroethylene and CF_2=CFO$(CF_2)_4SO_3H$. *Macromolecules* **2009,** *42* (15), 5774-5780; (b) Brandrup, J.; Immergut, E. H.; McDowell, W., *Polymer Handbook*. Wiley: 1975.

43. (a) Clark, E. S., The molecular conformations of polytetrafluoroethylene: forms II and IV. *Polymer* **1999,** *40* (16), 4659-4665; (b) Giffin, G. A.; Piga, M.; Lavina, S.; Navarra, M. A.; D'Epifanio, A.; Scrosati, B.; Di Noto, V., Characterization of sulfated-zirconia/Nafion® composite membranes for proton exchange membrane fuel cells. *Journal of Power Sources* **2012,** *198* (Supplement C), 66-75.

44. Page, K. A.; Cable, K. M.; Moore, R. B., Molecular Origins of the Thermal Transitions and Dynamic Mechanical Relaxations in Perfluorosulfonate Ionomers. *Macromolecules* **2005,** *38* (15), 6472-6484.

45. (a) Puskar, L.; Ritter, E.; Schade, U.; Yandrasits, M.; Hamrock, S. J.; Schaberg, M.; Aziz, E. F., Infrared dynamics study of thermally treated perfluoroimide acid proton exchange membranes. *Physical*

Chemistry Chemical Physics **2017,** *19* (1), 626-635; (b) Rey, I.; Johansson, P.; Lindgren, J.; Lassègues, J. C.; Grondin, J.; Servant, L., Spectroscopic and Theoretical Study of $(CF_3SO_2)_2N^-$ ($TFSI^-$) and $(CF_3SO_2)_2NH$ (HTFSI). *The Journal of Physical Chemistry A* **1998,** *102* (19), 3249-3258.

46. Atrazhev, V. V.; Astakhova, T. Y.; Sultanov, V. I.; Perry, M. L.; Burlatsky, S. F., Molecular Dynamic Study of Water-Cluster Structure in PFSA and PFIA Ionomers. *Journal of the Electrochemical Society* **2017,** *164* (12), F1265-F1271.

47. Negro, E.; Vittadello, M.; Vezzù, K.; Paddison, S. J.; Di Noto, V., The influence of the cationic form and degree of hydration on the structure of Nafion™. *Solid State Ionics* **2013,** *252* (Supplement C), 84-92.

48. Di Noto, V.; Gliubizzi, R.; Negro, E.; Vittadello, M.; Pace, G., Hybrid inorganic–organic proton conducting membranes based on Nafion and 5wt.% of M_xO_y (M=Ti, Zr, Hf, Ta and W): Part I. Synthesis, properties and vibrational studies. *Electrochimica Acta* **2007,** *53* (4), 1618-1627.

49. Klug, H. A., L. , *X-Ray Diffraction Procedures: For Polycrystalline and Materials*. 2nd ed.; John Wiley & Sons: New York, 1974.

50. (a) Adachi, M.; Navessin, T.; Xie, Z.; Frisken, B.; Holdcroft, S., Correlation of In Situ and Ex Situ Measurements of Water Permeation Through Nafion NRE211 Proton Exchange Membranes. *Journal of the Electrochemical Society* **2009,** *156* (6), B782-B790; (b) Adachi, M.; Navessin, T.; Xie, Z.; Li, F. H.; Tanaka, S.; Holdcroft, S., Thickness dependence of water permeation through proton exchange membranes. *Journal of Membrane Science* **2010,** *364* (1-2), 183-193; (c) Kreuer, K. D., The role of internal pressure for the hydration and transport properties of ionomers and polyelectrolytes. *Solid State Ionics* **2013,** *252* (0), 93-101.

51. (a) Caulk, D. A.; Brenner, A. M.; Clapham, S. M., A Steady Permeation Method for Measuring Water Transport Properties of Fuel Cell Membranes. *Journal of the Electrochemical Society* **2012,** *159* (9), F518-F529; (b) Vittadello, M.; Negro, E.; Lavina, S.; Pace, G.; Safari, A.; Di Noto, V., Vibrational

Studies and Properties of Hybrid Inorganic−Organic Proton Conducting Membranes Based on Nafion and Hafnium Oxide Nanoparticles. *The Journal of Physical Chemistry B* **2008,** *112* (51), 16590-16600.

52. (a) Masetti, G.; Cabassi, F.; Morelli, G.; Zerbi, G., Conformational Order and Disorder in Poly(tetrafluoroethylene) from the Infrared Spectrum. *Macromolecules* **1973,** *6* (5), 700-707; (b) Zerbi, G.; Sacchi, M., Dynamics of Polymers as Structurally Disordered Systems. Vibrational Spectrum and Structure of Poly(tetrafluoroethylene). *Macromolecules* **1973,** *6* (5), 692-699; (c) Piseri, L.; Powell, B. M.; Dolling, G., Lattice dynamics of polytetrafluoroethylene. *The Journal of chemical physics* **1973,** *58* (1), 158-171; (d) Hannon, M. J.; Boerio, F. J.; Koenig, J. L., Vibrational Analysis of Polytetrafluoroethylene. *The Journal of chemical physics* **1969,** *50* (7), 2829-2836; (e) Di Noto, V.; Boaretto, N.; Negro, E.; Pace, G., New inorganic–organic proton conducting membranes based on Nafion and hydrophobic fluoroalkylated silica nanoparticles. *Journal of Power Sources* **2010,** *195* (23), 7734-7742; (f) Quarti, C.; Milani, A.; Castiglioni, C., Ab Initio Calculation of the IR Spectrum of PTFE: Helical Symmetry and Defects. *The Journal of Physical Chemistry B* **2013,** *117* (2), 706-718; (g) Gruger, A.; Régis, A.; Schmatko, T.; Colomban, P., Nanostructure of Nafion® membranes at different states of hydration: An IR and Raman study. *Vibrational Spectroscopy* **2001,** *26* (2), 215-225.

53. Di Noto, V.; Longo, D.; Münchow, V., Ion-oligomer interactions in poly(ethylene glycol)400/$(LiCl)_x$ electrolyte complexes. *Journal of Physical Chemistry B* **1999,** *103* (14), 2636-2646.

54. Cooper, K. R., Progress Toward Accurate Through-Plane Ion Transport Resistance Measurement of Thin Solid Electrolytes. *Journal of the Electrochemical Society* **2010,** *157* (11), B1731-B1739.

55. Di Noto, V.; Giffin, G. A.; Vezzu, K.; Nawn, G.; Bertasi, F.; Tsai, T.-h.; Maes, A. M.; Seifert, S.; Coughlin, E. B.; Herring, A. M., Interplay between solid state transitions, conductivity mechanisms, and electrical relaxations in a [PVBTMA] [Br]-*b*-PMB diblock copolymer membrane for electrochemical applications. *Physical Chemistry Chemical Physics* **2015,** *17* (46), 31125-31139.

56. Di Noto, V.; Giffin, G. A.; Vezzù, K.; Piga, M.; Lavina, S., Broadband Dielectric Spectroscopy: A Powerful Tool for the Determination of Charge Transfer Mechanisms in Ion Conductors. In *Solid State Proton Conductors: Properties and Applications in Fuel Cells*, 2012; pp 109-183.

57. Savage, J.; Tse, Y.-L. S.; Voth, G. A., Proton Transport Mechanism of Perfluorosulfonic Acid Membranes. *The Journal of Physical Chemistry C* **2014,** *118* (31), 17436-17445.

TABLE OF CONTENT

Transport and Morphology of a Proton Exchange Membrane Based on a Doubly Functionalized Perflourosulfonic Imide Side Chain Perflourinated Polymer

Ahmet Kusoglu, Keti Vezzù, Govind Hegde, Graeme Nawn, Andrew R. Motz, Himanshu N. Sarode, Gregory M. Haugen, Yuan Yang, Soenke Seifert, Michael A. Yandrasits, Steven J. Hamrock, C. Mark Maupin, Adam Z. Weber, Vito Di Noto, and Andrew M. Herring.